JGR Solid Earth

RESEARCH ARTICLE
10.1029/2020JB019929

The Evolution of Mantle Plumes in East Africa

Sung-Joon Chang[1], Elodie Kendall[2], Anne Davaille[3], and Ana M. G. Ferreira[2,4]

[1]Department of Geophysics, Kangwon National University, Chuncheon, South Korea, [2]Department of Earth Sciences, University College London, London, UK, [3]Laboratoire FAST, CNRS/Université Paris Sud, Orsay, France, [4]CERIS, Instituto Superior Técnico, Universidade de Lisboa, Lisbon, Portugal

Key Points:
- Recent global tomography models show a continuous plume down to the core-mantle boundary beneath Kenya and a detached plume beneath Afar
- The interaction of the Afar plume with the Tethyan slab may be responsible for its detachment as shown in laboratory experiments
- A third plume between Kenya and Afar may have caused the Ethiopia-Yemen traps 30 Ma, now merging with the Afar plume

Supporting Information:
- Supporting Information S1

Correspondence to:
S.-J. Chang,
sjchang@kangwon.ac.kr

Citation:
Chang, S.-J., Kendall, E., Davaille, A., & Ferreira, A. M. G. (2020). The evolution of mantle plumes in East Africa. *Journal of Geophysical Research: Solid Earth*, *125*, e2020JB019929. https://doi.org/10.1029/2020JB019929

Received 6 APR 2020
Accepted 30 OCT 2020
Accepted article online 4 NOV 2020

Abstract Global tomography models show a large low-velocity anomaly extending from the core-mantle boundary (CMB) beneath South Africa to the upper mantle in East Africa. Although it is believed that this anomaly is linked to mantle upwellings that control key surface features of the African continent, its origin and evolution are still debated. Here we assemble geochemical and seismological constraints along with information from new seismic analyses and geodynamic laboratory experiments to propose that presently there are at least two different plume heads beneath Afar and Kenya that originated at the CMB. A third plume between Kenya and Afar may have caused the Ethiopia-Yemen traps 30 Ma, now merging with the Afar plume. We infer that the Afar plume is presently detached from the CMB probably because of an interaction with the subducted Tethyan slab and that it is likely a dying plume. This may imply that rifts along the Main Ethiopian Rift would fail by the loss of thermal sources, which consequently hampers continental breakup.

1. Introduction

Global tomography models consistently show two large low shear-velocity provinces (LLSVPs) in the lowermost mantle beneath the South Pacific and Africa (e.g., Chang et al., 2014; Lekic et al., 2012), which may have been stable over 200 Myr (Burke et al., 2008) due to their thermochemical nature (e.g., Garnero & McNamara, 2008). LLSVPs and associated mantle plumes may play a critical role in the evolution of Earth's life by inducing geomagnetic polarity reversals (Amit & Olson, 2015), mass extinctions (Courtillot & Olson, 2007), the breakup of supercontinents (Li & Zhong, 2009), and so forth. A large low-velocity anomaly rooted in the African LLSVP extends from the core-mantle boundary (CMB) beneath South Africa to the upper mantle beneath East Africa (e.g., Hansen et al., 2012; Ritsema et al., 1999). The formation of two domes in East Africa, the Ethiopian and the Kenyan plateaux, is often attributed to a buoyancy force due to upwellings associated with this low-velocity anomaly (Ritsema et al., 1999), yielding a large amount of dynamic topography (Lithgow-Bertelloni & Silver, 1998). The East African Rift system (EARS) within these domes is the locus of rifting activity in one of three arms of the Afar triple junction, causing continental breakup of the African plate. Although there is a consensus on the role of mantle upwellings in the formation of the EARS and of the two plateaux (e.g., Daradich et al., 2003; Hansen et al., 2012; Lin & van Keken, 2005; Ritsema et al., 1999), there are still key questions that remain unanswered, notably, how many plumes (or plume heads) are responsible for the formation of the EARS and the two plateaux? Why are there discrepancies between volcanism in the two plateaux such as different chemical compositions, timing, eruption styles, and hotspot tracks? Can there be a single plume in the region that is tilted as much as ~45° and causing all the volcanism in the EARS? Is the boundary of the African LLSVP at the CMB fixed?

Several geodynamical models have been proposed to explain the formation of the EARS and the two plateaux as summarized in Figure 1. Many geophysical studies including regional and global tomography models (e.g., Benoit, Nyblade, Owens, et al. 2006; Benoit, Nyblade, & VanDecar, 2006; Hansen & Nyblade, 2013; Hansen et al., 2012; Ritsema et al., 1999) and geodynamical simulations using buoyancy forces inferred from tomography models (e.g., Daradich et al., 2003; Moucha & Forte, 2011) have supported the idea of one single large, tilted upwelling from beneath South Africa to Afar (a.k.a. "the African superplume"; Figure 1a). This upwelling may be responsible for all the volcanism along the EARS through channeled mantle flow along thin lithosphere (Ebinger & Sleep, 1998; Figure 1a). Other geochemical, geodynamical, and seismological studies have suggested that the large low shear-velocity anomaly observed in tomography models beneath East Africa down to the CMB actually comprises two

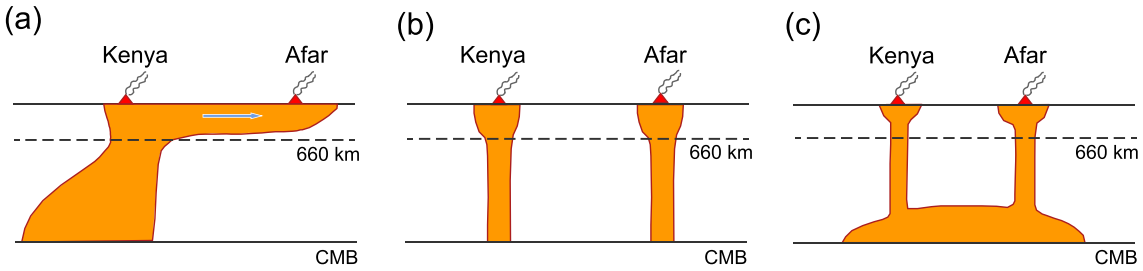

Figure 1. Conceptual plume models beneath East Africa. (a) Superplume model. (b) Two separate plume model with distinct sources at the CMB. (c) Two plume heads from a common source at the CMB.

separate plumes corresponding to the two plateaux in East Africa (e.g., Chang & van der Lee, 2011; Davaille et al., 2005; George et al., 1998; Lin et al., 2005; Montelli et al., 2004; Pik et al., 2006; Rogers et al., 2000; Schubert et al., 2004; Figure 1b). On the other hand, some geochemical and seismological studies suggested that the two plateaux were formed due to two plume heads sharing a common plume source in the lower mantle (Halldórsson et al., 2014; Montelli et al., 2006; Nelson et al., 2012; Figure 1c). Recently,

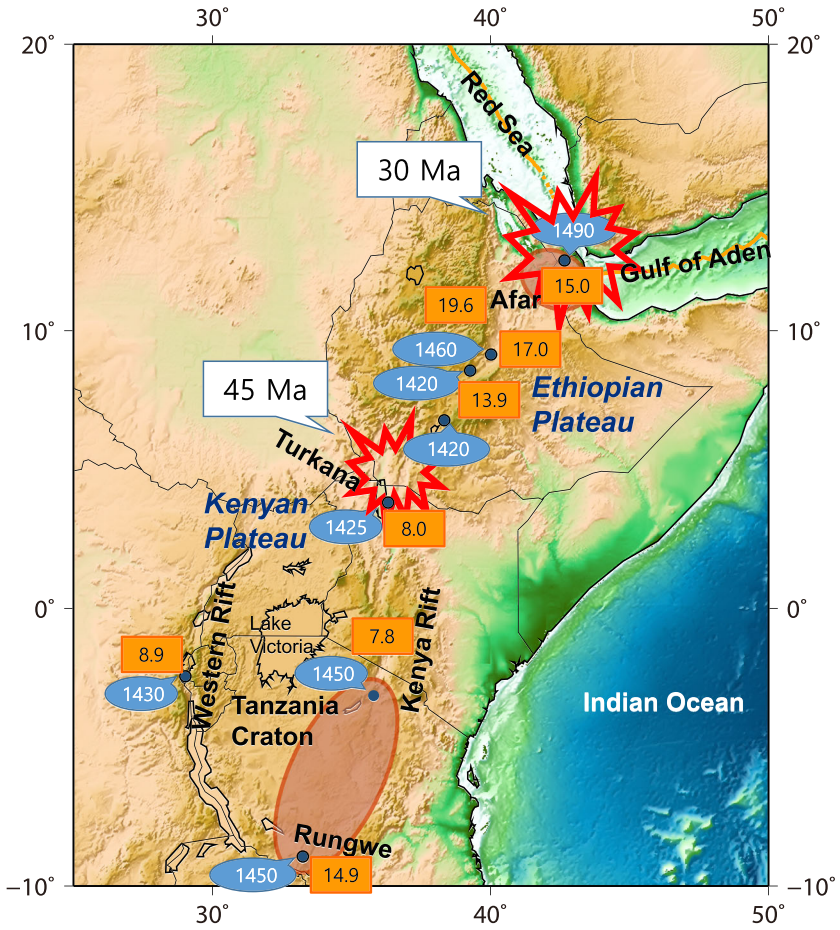

Figure 2. Summary of geochemical information in the EARS. The two red explosion symbols indicate the locations of the initial basalt eruptions in the Ethiopian (30 Ma) and the Kenyan (45 Ma) plateaux (Nelson et al., 2012). Numbers enclosed by cyan circles represent mantle potential temperatures for lava erupted since 10 Ma (Rooney, Herzberg, & Bastow, 2012), and the two brown ellipses show the spatial distribution of the highest mantle potential temperatures in each plateau. The numbers enclosed by orange squares show measured $^{3}He/^{4}He$ ratios (R/R_A notation) (Hilton et al., 2011).

some regional tomography studies found a cluster of secondary thin plumes in the upper mantle (Civiero et al., 2015, 2016), which would be imaged as one single large plume in global tomography models due to their limited resolution (typically around 1,000 km).

Here we compile geochemical and geophysical data from the EARS and interpret them together with new constraints from seismology and geodynamics, notably from independent seismic waveform modeling and geodynamic laboratory experiments. In order to satisfy all the observations, we propose that the low-velocity anomaly beneath East Africa observed in global tomography models currently consists of at least two separate plumes, the Afar plume and the Kenya plume, which originated from the African LLSVP at the CMB. We also infer that a third plume between Kenya and Afar may have caused the Ethiopia-Yemen traps 30 Ma but is now merging with the Afar plume. Moreover, we propose that the Afar plume is detached from the CMB, likely a dying plume, hampering continental breakup of the African plate.

2. Constraints From Geochemical Information

In the EARS, the basalts from the Ethiopian and the Kenyan plateaux have several distinct geochemical characteristics, timing, and eruption styles from each other. The first basalt eruption occurred in southern Ethiopia and in the northern Turkana depression 45 Ma (Ebinger et al., 1993), and it has continued until now on an episodic basis, moving southward to central Tanzania (George et al., 1998; Figure 2). In contrast, massive flood basalts (~500,000 km^2) were produced in northern Ethiopia, Eritrea, and Yemen approximately 30 Ma over a short period of 1 Myr (Hofmann et al., 1997) leading to the emplacement of the Ethiopia-Yemen traps. The basalts in the Ethiopian plateau show high $^3He/^4He$ ratio (up to 19.6 R_A; R_A is isotope helium ratio in the atmosphere), which indicates that they originate from lower mantle reservoirs (Marty et al., 1996). In contrast, basalts in the Kenyan plateau show mid-ocean ridge basalt (MORB)-type low $^3He/^4He$ ratio of ~8 R_A (Pik et al., 2006). Furthermore, distinct isotopic compositions were also found in Sr, Nd, Pb, and Hf isotope data between basalts from Ethiopia and Kenya, which require different mantle sources (Furman et al., 2006; Locke et al., 2008; Rogers et al., 2000; Rooney, Hanan, et al., 2012). Based on new Os and Hf isotope data in addition to aforementioned isotopic distinctions, Nelson et al. (2012) proposed that basalts in Ethiopia contain "C"-like composition, while "HIMU"-like composition is contained in basalts in the Turkana depression and in the Kenya Rift. Given these differences of isotope components, timing, and eruption styles between the Ethiopian and the Kenyan plateaux, two mantle upwellings from different sources have been attributed to the origin of the two plateaux (e.g., George et al., 1998; Pik et al., 2006; Rogers et al., 2000). The decrease of proportion of plume material along the Main Ethiopian Rift southwestwardly (Rooney, Hanan, et al., 2012), which may indicate mantle flow starting from Afar, also possibly supports the separate impingement of different plumes. However, in order to reconcile their results with those from geophysical studies supporting the African superplume model, some geochemistry studies (Furman et al., 2006; Nelson et al., 2012) attributed the distinct isotope compositions to heterogeneity of the African superplume. Nelson et al. (2012) proposed that mixing of ancient recycled oceanic crust and "C"-dominant source at the CMB can account for the observed "HIMU" composition in Kenya, suggesting that the heterogeneous African superplume is responsible for different compositions in the two pleateaux.

The distinct isotope observations between Ethiopia and Kenya were challenged by the discovery of high $^3He/^4He$ ratios up to 14.9 R_A in the southernmost part of the Kenyan plateau, Rungwe, similar to the Ethiopian plateau (Hilton et al., 2011; Figure 2). Such high $^3He/^4He$ ratios in Rungwe may imply that the entire EARS has been affected by a single plume source with high $^3He/^4He$ ratios, but the Tanzania craton in the Kenyan plateau has diluted $^3He/^4He$ ratios, thereby producing "HIMU"-like composition in the Kenyan plateau. The waning influence of the Tanzania craton in the southernmost of the Kenyan plateau may be responsible for the reappearance of high $^3He/^4He$ ratios in Rungwe. Furthermore, Halldórsson et al. (2014) found that a single He-Ne composition can characterize the entire EARS, by mixing a plume component with depleted MORB mantle or subcontinental lithospheric mantle, suggesting that the two plateaux in East Africa represent two different plume heads originating from the same deep-rooted plume source. Therefore, geochemical evidence seems to rule out the two separate plume model with distinct sources at the CMB (Figure 1b) as a potential hypothesis to explain the isotope characteristics of basalts from East Africa, suggesting a common plume source for the entire region, the African superplume (Figure 1a), or two plume heads from a common source at the CMB (Figure 1c).

Table 1
Details of Recent Global Tomography Models

Models	Data	Parameterization	Modeling scheme
S362ANI (Kustowski et al., 2008)	Fundamental-mode phase velocities (35–150 s), long-period waveforms (T > 50 s), ~140,000 body-wave traveltimes[a]	New 1-D reference model STW105, nominal lateral resolution: ~1,000 km, 16 depth splines	Ray theory
S40RTS (Ritsema et al., 2011)	Approximately 27 M fundamental and overtone phase velocities (40–275 s), ~460,000 body-wave traveltimes, ~84,000 even-degree self-coupling splitting functions	1-D reference model PREM, nominal lateral resolution: ~1,000 km, 21 depth splines	Ray theory
SAVANI (Auer et al., 2014)	Approximately 12 M fundamental and overtone phase velocities (25–370 s), ~510,000 body-wave traveltimes	1-D reference model PREM, variable block parameterization (nominal lateral resolution: 300–1,000 km), 28 vertical layers	Ray theory
SEMUCB-WM1 (French & Romanowicz, 2014)	Approximately 250,000 body waveforms (T > 32 s), ~200,000 surface waveforms (T > 60 s)	Own 1-D reference model, nominal lateral resolution: ~500 km, 20 depth splines	Spectral element method for forward modeling, nonlinear asymptotic coupling theory for inverse modeling
SGLOBE-rani (Chang et al., 2015)	1.6 M fundamental mode group-velocity data (16–150 s), ~41 M fundamental and overtone phase-velocity data (25–374 s), ~420,000 traveltime data	1-D reference model PREM, nominal lateral resolution: ~1,200 km, 21 depth splines, simultaneous inversion for crustal and mantle structure	Ray theory
SEISGLOB2 (Durand et al., 2017)	Approximately 22 M fundamental and overtone phase-velocity data (40–240 s), normal mode self-coupling (9,214) and cross-coupling (643) coefficients, ~100,661 traveltime data	1-D reference model PREM, nominal lateral resolution: ~1,000 km, 21 depth splines	Ray theory

[a]The numbers of phase velocities and waveforms used for S362ANI are not clearly stated in Kustowski et al. (2008) for all wave periods used. For the wave periods reported in Kustowski et al. (2008), the numbers of measurements are 1 to 3 orders of magnitude smaller than those for the other models.

The basalts from the Ethiopian and the Kenyan plateaux also exhibit distinct thermal properties from each other. Rooney, Herzberg, and Bastow (2012) measured mantle potential temperatures from basalts in East Africa and found that the highest mantle temperatures from old basalts (40–10 Ma) in both plateaux are observed near the locations of the first eruptions (explosion marks in Figure 2). When analyzing recent basalts (<10 Ma), they found a similar location of the highest mantle potential temperatures for the Ethiopian plateau, whereas the highest temperatures from recent basalts in the Kenyan plateau were observed further south in Rungwe and in the southern Kenya Rift (brown ellipses in Figure 2). The latter is compatible with the northeastward absolute motion of the African plate (George et al., 1998). However, the region with the highest mantle temperature within the Ethiopian plateau did not move southward unlike its Kenyan counterpart. In section 6, we will discuss that these features can be explained by the presence of multiple plumes in the region.

3. Constraints From Recent Global Tomography Models

In the past decade, several global tomography models have been built using different data sets and modeling strategies (e.g., distinct forward and inverse modeling schemes, parameterization, and data sets as shown in Table 1), and they share common large-scale low-velocity perturbations near the CMB (LLSVPs). Figure 3 shows cross sections and depth maps using six global shear wave velocity tomography models: (i) S362ANI (Kustowski et al., 2008), (ii) S40RTS (Ritsema et al., 2011), (iii) SAVANI (Auer et al., 2014), (iv) SEMUCB-WM1 (French & Romanowicz, 2014), (v) SGLOBE-rani (Chang et al., 2015), and (vi) SEISGLOB2 (Durand et al., 2017). All models clearly show a strong, tilted low-velocity anomaly of about −1% from the CMB beneath South Africa to the mantle transition zone (MTZ) beneath Tanzania and Kenya (Figures 3a–3c and 3g–3i). In contrast, directly beneath Afar, the models show no or very weak low-velocity anomalies in the lowermost mantle (Figures 3d–3f and 3j–3l). SEISGLOB2 shows a smoother

and broader pattern of low-velocity anomalies in the lowermost mantle beneath East Africa than in the other models, which is possibly due to the fact that this model does not use diffracted *S* waves that are sensitive to the CMB depth (Durand et al., 2017). Nevertheless, the anomalies in SEISGLOB2 beneath Afar are weaker than beneath Kenya and are not connected to low-velocity anomalies in the upper mantle.

In the upper mantle, all the models except for S362ANI seem to show two distinct low-velocity anomalies beneath Afar and Kenya, which are more clearly shown in isosurfaces of low-velocity anomalies (Figure 4). We also added isosurfaces from high-resolution regional upper-mantle models by Emry et al. (2019) and Celli et al. (2020; AF2019). Emry et al. (2019) built a continental-scale upper mantle model by using ambient noise full-waveform tomography for a period range of 7 to 340 s. AF2019 is a global tomography model of the upper mantle constructed by using over 1.2 million seismic waveforms, but its regularization is tuned to optimize the resolution in Africa (and hence, we refer to it as a high-resolution regional model). Both studies included newly available waveforms from the AfricaArray (Nyblade et al., 2011). The high-resolution regional models also show multiple segments of low-velocity anomalies in the upper mantle, supporting the features observed in the global models except for S362ANI. Both regional models show three segments of low-velocity anomalies beneath East Africa (not two as in the global tomography models). These features will be discussed in section 6 in more detail. Interestingly, two separate low-velocity anomalies in the global models are also observed in the uppermost lower mantle (Figures 3 and 5), which may imply that the two low-velocity anomalies observed in the upper mantle may be upwelling from the lower mantle separately, that is, that they are not secondary plumes from a single large plume stagnant in the MTZ. Hence, global tomography models clearly show a morphology of two separate low-velocity anomalies beneath Kenya and Afar down to at least the uppermost lower mantle, which is against the idea of a single large plume in the region (Figure 1a).

It is also noteworthy that, apart from Model S362ANI, the other global models show strong low-velocity anomalies up to −1.8% in the uppermost lower mantle beneath Afar from ~660 to ~1,000 km depth (ellipses in Figures 3b, 3c, and 3g–3i). We will test whether this morphology is robustly resolved in tomography models later in section 4 and will discuss it in section 6. Among all models considered, S362ANI is the smoothest one, and it was built using a smaller data set than the others (see Table 1), which may at least partly explain why it does not show clearly distinct mantle velocity anomalies between Afar and Kenya.

4. Robustness of Seismic Structure Beneath East Africa in Global Tomography Models

In the next subsections, we perform several types of robustness tests such as K-means clustering analyses, Backus-Gilbert resolution tests, and waveform modeling in order to assess the robustness of low-velocity anomalies beneath East Africa in global tomography models.

4.1. K-Means Clustering Analysis

In the previous section, we showed that recent global tomography models reveal two separate low-velocity anomalies beneath Kenya and Afar in the upper mantle and in the uppermost lower mantle. In order to test the statistical significance of the two distinct low-velocity anomalies that go down to the uppermost lower mantle, we perform K-means clustering analyses using the six global tomography models aforementioned in a box around the region of interest (Figure 6). We assemble depth slices on a $2° \times 2°$ horizontal grid from 210 to 660 km depth and from 670 to 1,000 km depth at an interval of 10 km to consider the distributions of the low-velocity anomalies in the upper mantle and in the uppermost lower mantle separately. We do not include depth slices shallower than 210 km to reduce the influence of tectonic features such as cratons on the analysis. Then, we apply the K-means clustering algorithm (e.g., Chang & Ferreira, 2019; Ferreira et al., 2019; Lekic et al., 2012; MacQueen, 1967) to the two collections of depth slices from the six global tomography models. By using this technique, we divide the set of shear wave velocity profiles into K groups of similar velocity profiles.

Figure 6 shows the results obtained with $K = 7$. We use $K = 7$ because two separate lowest-velocity anomalies begin to appear for all global models except for S362ANI with $K \geq 7$. The study region covers a wide region including diverse tectonic features from cratons to oceanic crust, so we need at least $K = 7$ to discriminate the lowest-velocity anomalies as shown in Figure 4. Apart from the S362ANI model (which is the

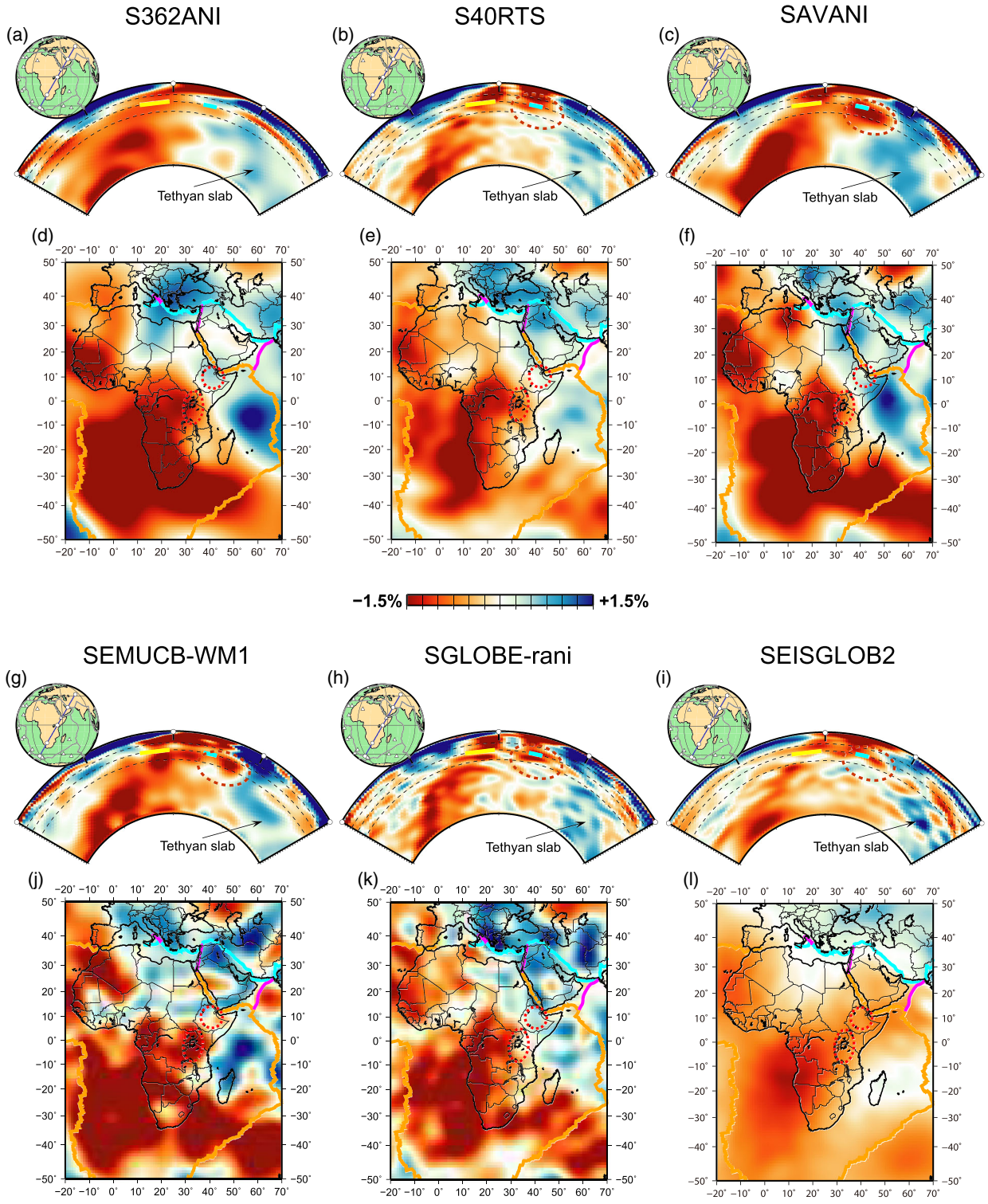

Figure 3. Cross sections and depth slices at 2,800 km from the Models S362ANI (Kustowski et al., 2008), S40RTS (Ritsema et al., 2011), SAVANI (Auer et al., 2014), SEMUCB-WM1 (French & Romanowicz, 2014), SGLOBE-rani (Chang et al., 2015), and SEISGLOB2 (Durand et al., 2017). (a–c and g–i) Cross sections along the EARS. Black dashed lines indicate 410, 660, and 1,000 km depths. The yellow lines at 660 km depth beneath Tanzania represent the thin MTZ reported by Mulibo and Nyblade (2013), while the cyan lines beneath Afar correspond to the hydrous MTZ reported by Thompson et al. (2015) and Reed et al. (2016). Strong low-velocity anomalies in the uppermost lower mantle beneath Afar are indicated by dotted red ellipses. Tick marks in cross sections are indicated every 30°. (d–f and j–l) Depth slices of the six models at 2,800 km. Locations of the Ethiopian and the Kenyan plateaux are indicated by dotted red ellipses.

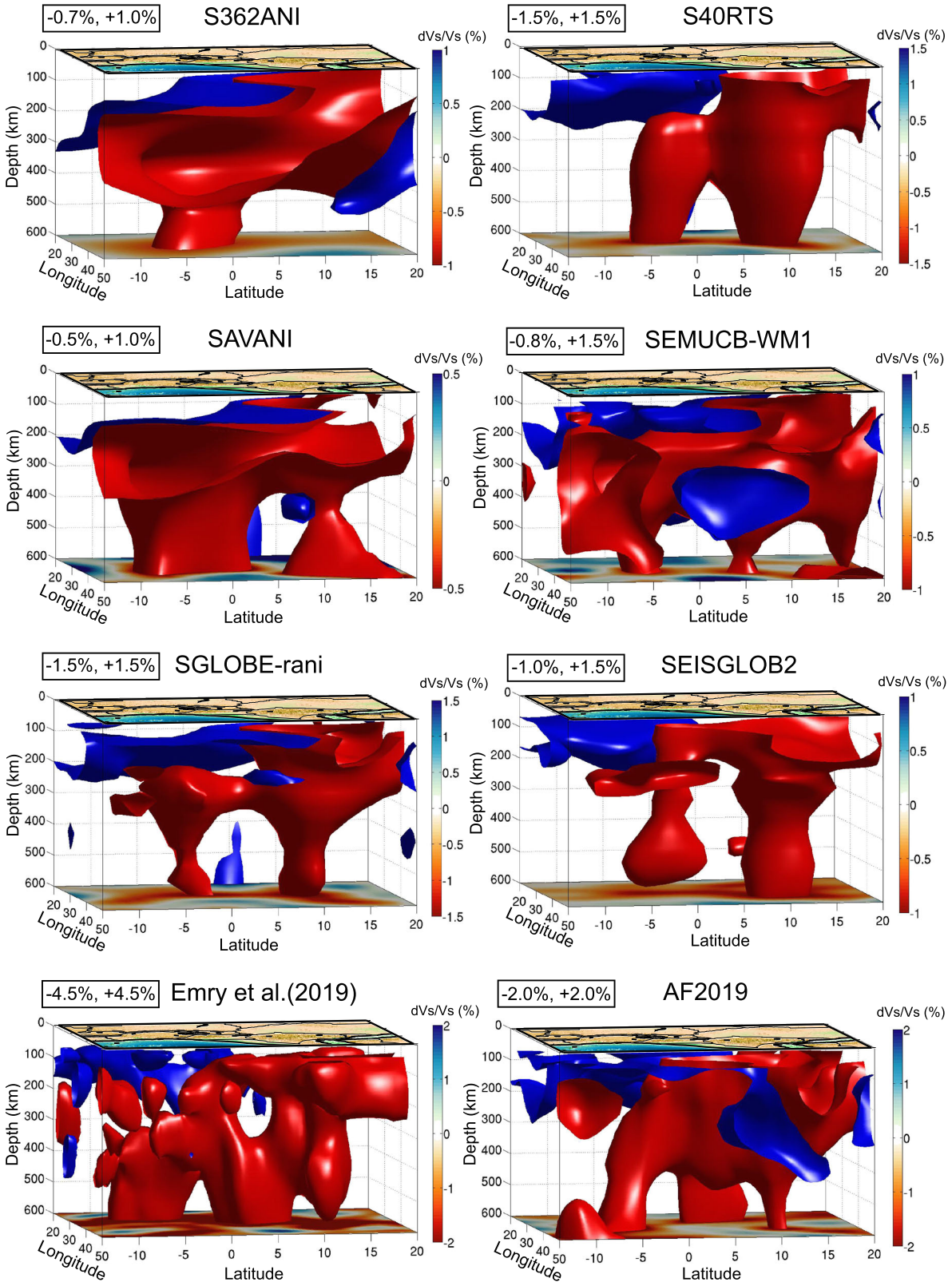

Figure 4. Isosurfaces of low- and high-velocity anomalies in the upper mantle beneath East Africa from six global tomography models and two regional models (Emry et al., 2019; AF2019 by Celli et al., 2020). We used different values for isosurfaces in each model to clearly show the lowest-velocity anomalies, which are noted on the top left of each subplot.

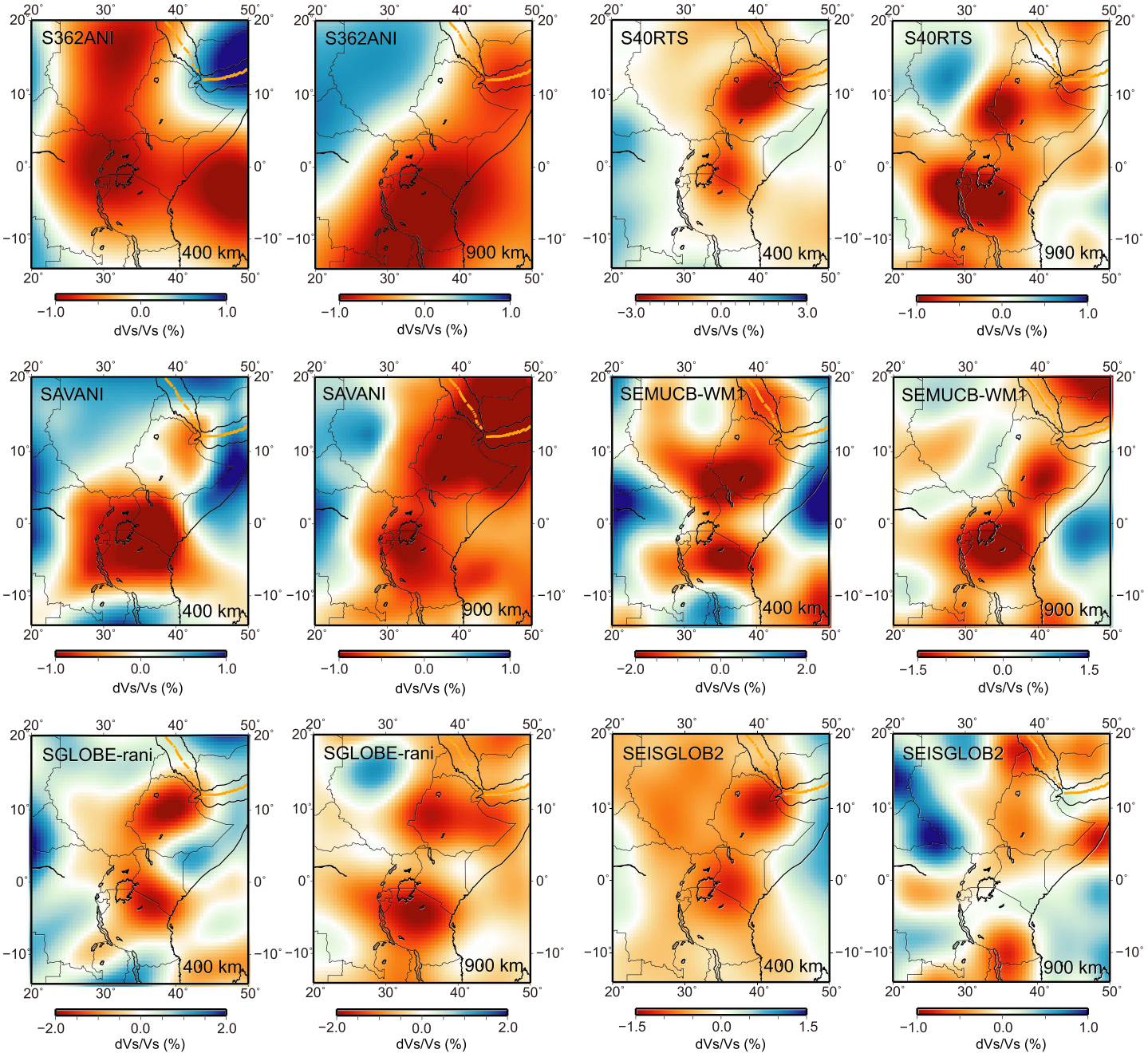

Figure 5. Depth slices at 400 and 900 km from the six global tomography models considered in this study.

smoothest one, as discussed in the previous section), the other five global models show separate lowest-velocity anomalies (red colors in Figure 6) beneath Kenya and Afar in the upper mantle (S40RTS, SAVANI, SGLOBE-rani, and SEISGLOB2) and in the uppermost lower mantle (S40RTS, SEMUCB-WM1, SGLOBE-rani, and SEISGLOB2). Among the five recent global models, only SAVANI shows one single red region in the uppermost lower mantle. However, the shape of the region in orange color (the second lowest-velocity anomaly) seems to depict two separate low-velocity anomalies connected in between. Two separate lowest-velocity anomalies in the uppermost lower mantle are observed in SAVANI from K = 10. SEMUCB-WM1 also shows one single large low-velocity anomaly in the upper mantle (Figure 6), but when comparing with the depth slice in Figure 5, it seems that two or three lowest-velocity anomalies are connected due to a low K number. The single lowest-velocity anomaly begins to divide into two from K = 9.

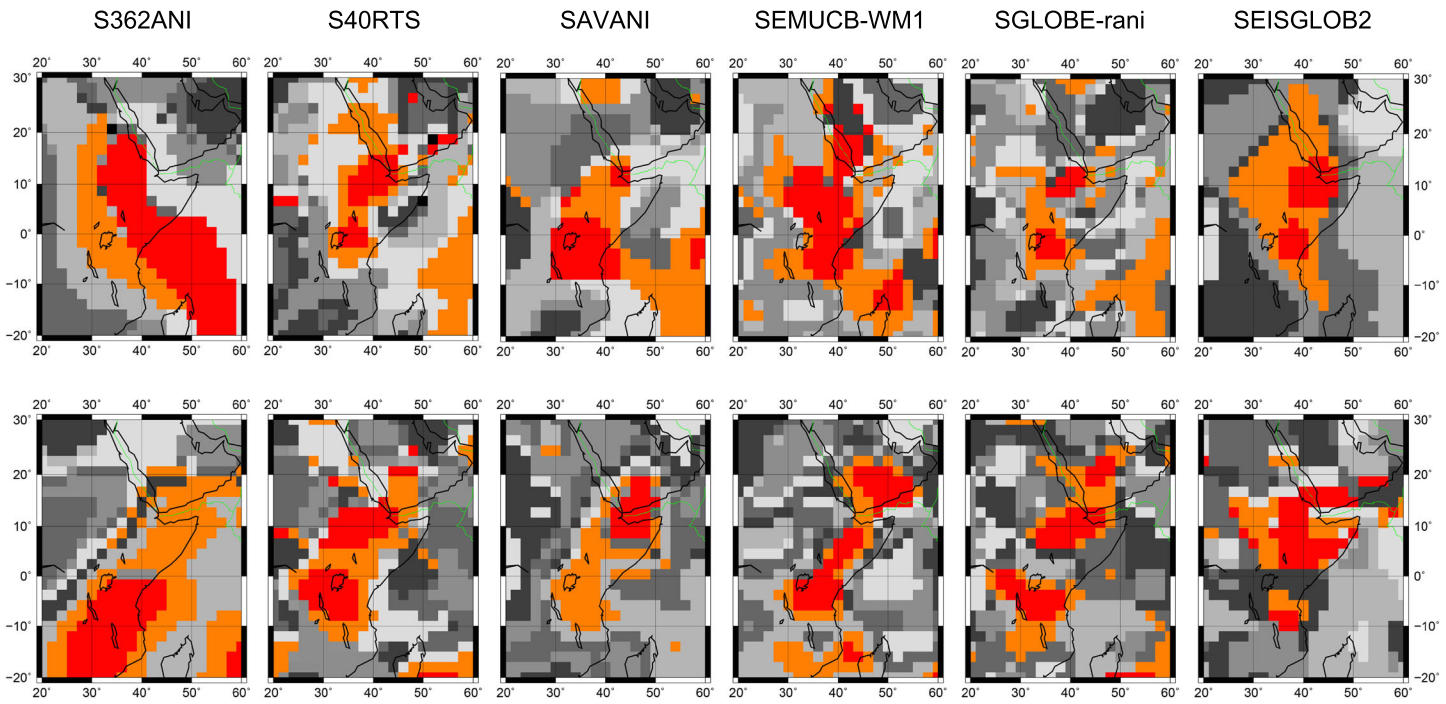

Figure 6. K-mean clustering tests for the distributions of shear wave velocity anomalies in the six global tomography models considered in this study at 210–660 (top) and 670–1,000 km depths (bottom) with K = 7. The strongest and second strongest low-velocity anomalies are indicated by red and orange colors, respectively. Other regions are randomly colored in gray scale.

Therefore, our K-mean clustering analysis suggests that recent global tomography models except for S362ANI unanimously show two separate mantle plumes beneath Kenya and Afar down to the uppermost lower mantle.

4.2. Model Resolution and Effects of Regularization

Among the six global tomography models considered in this study, we perform Backus-Gilbert resolution tests (Backus & Gilbert, 1968) of SGLOBE-rani, since we know all the details of its construction and we have computed its resolution matrix (Chang et al., 2015). Backus-Gilbert averaging kernels describe the model's spatial resolving power. Ideally, these kernels should be delta functions, but in practice, they are broad because of incomplete data coverage, regularization, and model parameterization. We carry out these tests for upper mantle depths from 190 to 600 km depth beneath Afar, Turkana, and Kenya to assess how well resolved is the morphology of the Afar and the Kenya plumes observed in the model's upper mantle (supporting information Figures S1 and S2). As expected, there is a tendency for the Backus-Gilbert kernels to broaden with depth (Figure S1), but there are no substantial differences in the model's resolving power for the different regions considered, which means that the weak anomalies beneath Turkana are not caused by poor data coverage. The lateral extent of the Backus-Gilbert kernels for the three regions tends to spread out with depth, but they are almost identical between regions without substantial differences between them (Figure S2). We also perform resolution tests for the lower mantle depths from 950 to 2,580 km depth beneath Afar, Kenya, and South Africa (Figures S3 and S4). Figure S3 shows that SGLOBE-rani has a good vertical resolution in the lower mantle beneath Africa, showing relatively narrow Backus-Gilbert kernels with a width of ~400–600 km. The lateral extent of the kernels in the lower mantle is also very similar for the regions considered (Figure S4), as in the upper mantle. Therefore, these tests assure that the differences observed in the tomography models between the Kenya and the Afar plumes in the upper and lower mantle do not result from biases in model resolution between the two regions. The Afar plume is robustly imaged to be discontinuous, with no clear low-velocity signature below the uppermost lower mantle. Otherwise, it may have a weak and/or too thin plume tail in that region beyond the models' resolution (e.g., Goes et al., 2004; Maguire et al., 2016, 2018; Styles et al., 2011).

In order to further evaluate the resolving power of SGLOBE-rani in a more realistic way, we also perform a synthetic inversion test using the same parameterization and data set configuration as in the construction of SGLOBE-rani and with SGLOBE-rani as input model (Figure S5). Two strong low-velocity anomalies beneath Afar and Kenya are well resolved in the upper and the uppermost lower mantle. Therefore, this further confirms that SGLOBE-rani has a good data coverage to discern two separate low-velocity anomalies beneath East Africa as shown in the Backus-Gilbert kernel tests.

We also test the influence of individual data sets on the resolved anomalies to assess the possibility of model artifacts due to data set bias. To build SGLOBE-rani, we used two main seismic data sets: surface-wave dispersion measurements and teleseismic body-wave traveltime data. Surface-wave data have a good vertical resolution but can have lateral smearing along raypaths in the case of a dearth of data. In contrast, body-wave traveltimes have a good lateral resolution but are prone to vertical smearing in the shallow depth due to near-vertical ray incidence. We carry out inversions with surface-wave data only and with traveltime data only (Figure S6). The results at 100–400 km depths show the complementary nature of the two data sets. Surface-wave data have a good resolution down to 200 km depth but poorer resolution from 300 km depth and below and vice versa for traveltime data. It is notable that both data sets independently require two distinct low-velocity anomalies at 200 km depth, which indicates that the two observed distinct anomalies are not an artifact due to, for example, the strong influence of traveltime data caused by limited data coverage. We also note that the body-wave data coverage for Africa is not limited to seismic stations installed there, because we used not only the direct *S* phase but also multiply reflected phases such as SS, SSS, ScS2, ScS3, sSS, sSSS, and sSCS2 in the construction of SGLOBE-rani (Chang et al., 2015). In addition, since we used events occurring in Africa, that also improves the data coverage of the region.

Finally, we examine the dependence of SGLOBE-rani on model regularization. As explained in Chang et al. (2015), norm damping is used in the construction of SGLOBE-rani. We obtain five different models using exactly the same data set and modeling approach used to build SGLOBE-rani but with different levels of norm damping in Figure S7 (the roughness of the models increases from the top to the bottom). As norm damping increases, the model's effective (free) number of parameters decreases, which is given by the trace of the resolution matrix. Although the two low-velocity anomalies beneath Kenya and Afar become weaker or stronger according to the roughness of the models, they prevail throughout the upper mantle and uppermost lower mantle regardless of regularization, thereby indicating that the two plumes are robustly resolved. We cannot guarantee that other global models also have similar resolution in all regions, as in SGLOBE-rani. However, by showing that at least SGLOBE-rani has enough resolution to detect separate low-velocity anomalies in the whole mantle beneath East Africa, we believe that this adds strength to our arguments. Furthermore, the other models except S362ANI use similar data sets to SGLOBE-rani, and so we think that the other global models may have similar resolving powers.

4.3. Seismic Waveform Modeling

In order to further assess the robustness of the low-velocity anomalies in the tomography models in an independent way, we compute theoretical seismograms using the spectral element method (Komatitsch & Tromp, 2002a, 2002b) for three different mantle models combined with the global crustal model CRUST2.0 (Bassin et al., 2000): (i) S362ANI (Kustowski et al., 2008), (ii) S40RTS (Ritsema et al., 2011), and (iii) SGLOBE-rani (Chang et al., 2015). These models cover the range of tomographic observations in East Africa discussed in section 3, from showing distinct shear wave speed anomalies beneath Afar and Kenya (S40RTS and SGLOBE-rani) to depicting no clear differences between the two regions (S362ANI). In particular, S40RTS and SGLOBE-rani share the common feature of low-velocity anomalies in the MTZ and the uppermost lower mantle underneath Afar, which does not appear in S362ANI (Figures 4–6). We use these tomography models among the six global models in section 3 because these three models represent the various morphologies of low-velocity anomalies beneath East Africa and it is not our intention to pick the “best” models out of the six models.

We analyze direct, radial-component *S* waveforms filtered between 20 and 30 s from available temporary and permanent seismic networks in the region (Tables S1 and S2). We use 30 shallow (depth < 50 km) earthquakes with magnitude Mw 4.9–6.3 (Table S3) and within epicentral distances of 19–50° (Figure S8), since direct *S* phases in that distance range travel through the transition zone and uppermost lower mantle

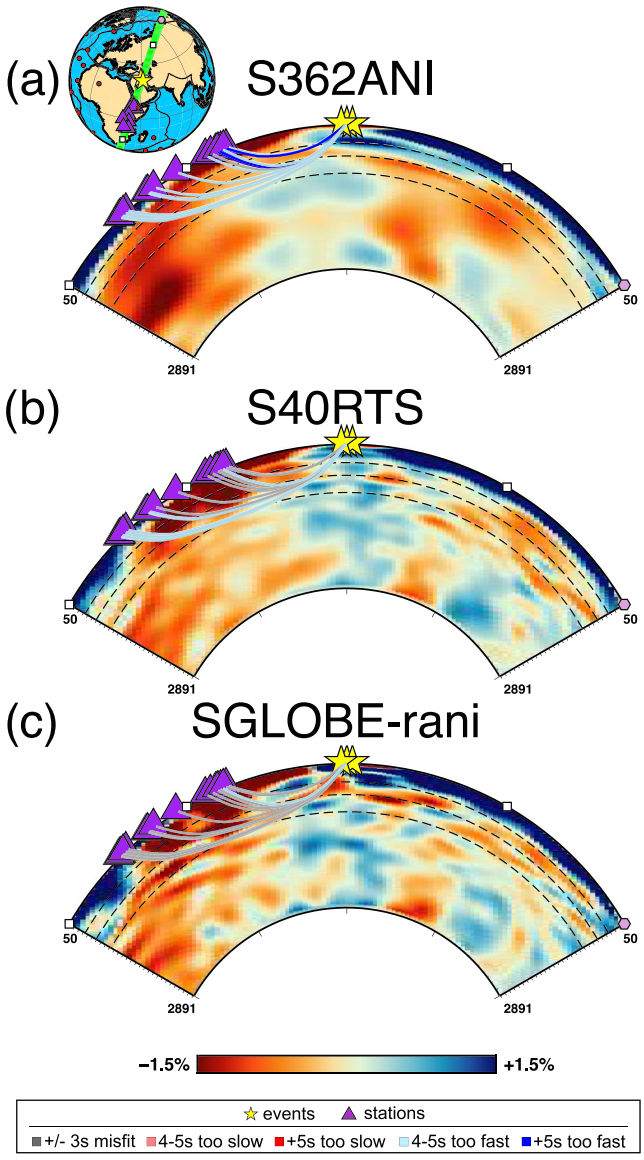

Figure 7. Direct *S* wave raypaths from three events in the Iran-Iraq border region (Table S3) along vertical cross sections from (a) S362ANI, (b) S40RTS, and (c) SGLOBE-rani. Raypaths are color coded to indicate the traveltime differences between observations and synthetics according to the legend at the bottom. Yellow stars and purple triangles indicate events and seismic stations, respectively. Black dashed lines indicate 410, 660, and 1,000 km depths. Ticks are marked every 30°.

where the wide low-velocity anomalies are observed (Figure 7). Figures 8a–8c show all the raypaths sensitive to the MTZ and uppermost lower mantle structure beneath Afar, which are color coded by the corresponding traveltime differences between the observed and theoretical waveforms. While S40RTS and SGLOBE-rani show a good data fit with traveltime differences within 2 s, S362ANI generates synthetic waveforms much faster than the observations. Illustrative waveform comparisons between observations and synthetics from the three models for an Mw 5.7 event in the Iran-Iraq border region (red star) are presented in Figure 8d. The synthetic waveforms for the Model S362ANI are systematically faster than the observations. We investigate these systematic fast arrivals in S362ANI in detail by depicting color-coded raypaths from three events in the Iran-Iraq border region (see Figure 8 and Table S3) in a vertical transect to be compared with those from the other two models (Figure 7). Corresponding phase misfits (traveltime differences) are shown in Figure S9. It is remarkable that the largest phase misfits of 7 s are observed only in Afar within epicentral distances of 25° for S362ANI (Figure S9), which seem to be caused by a lack of strong low-velocity anomalies in the MTZ and the uppermost lower mantle beneath Afar (Figure 7). In contrast, the phase misfits obtained for the other models are confined within 4 s in Afar, being almost half of the misfits for S362ANI. However, the misfits are down to 5 s in S362ANI beyond epicentral distances of 30°, which are comparable to, but still worse than misfits for the other models. This reduction of misfits for S362ANI for longer distances may be due to deeper raypaths that are less sensitive to the strong low-velocity anomalies in the MTZ and the uppermost lower mantle beneath Afar. It also suggests that S362ANI's large misfits are not mainly controlled by its regularization. We also examine the influence of hypocenter uncertainties on our results by computing synthetic seismograms using perturbed hypocenters of the red star event in Figure 8 (Figure S10). We perturb the hypocenter by 20 km laterally or vertically according to reported errors (~20 km) in Global Centroid Moment Tensor (GCMT) locations (Weston et al., 2011). The data misfit residuals from the three models due to the perturbed hypocenters are different within 1 s between all the models. This indicates a small influence of hypocenter uncertainties on our results that S362ANI predicts much faster arrivals in Afar compared with the other models. Hence, our independent seismic waveform analyses demonstrate that seismic observations require low-velocity anomalies in the MTZ and the uppermost lower mantle beneath Afar, which is against the idea of a single large plume in the region (Figure 1a).

5. Geodynamical Constraints on Morphology and Time Dependence of Plumes

The previous section clearly highlighted two distinct seismic low-velocity anomalies beneath Kenya and Afar and that the Afar anomaly goes down to the uppermost lower mantle. This is not compatible with the idea of a single large plume rising from the CMB beneath South Africa, spreading laterally in the upper mantle and then feeding the surface volcanism in East Africa.

The existence of several plumes beneath Africa is predicted by the physics of mantle convection. Hot mantle plumes are one of the main features of mantle thermal convection (for reviews, see Davaille & Limare, 2015; Schubert et al., 2001). In a system cooled from above and heated from below, the intensity of convection and the convective patterns are controlled by the Rayleigh number

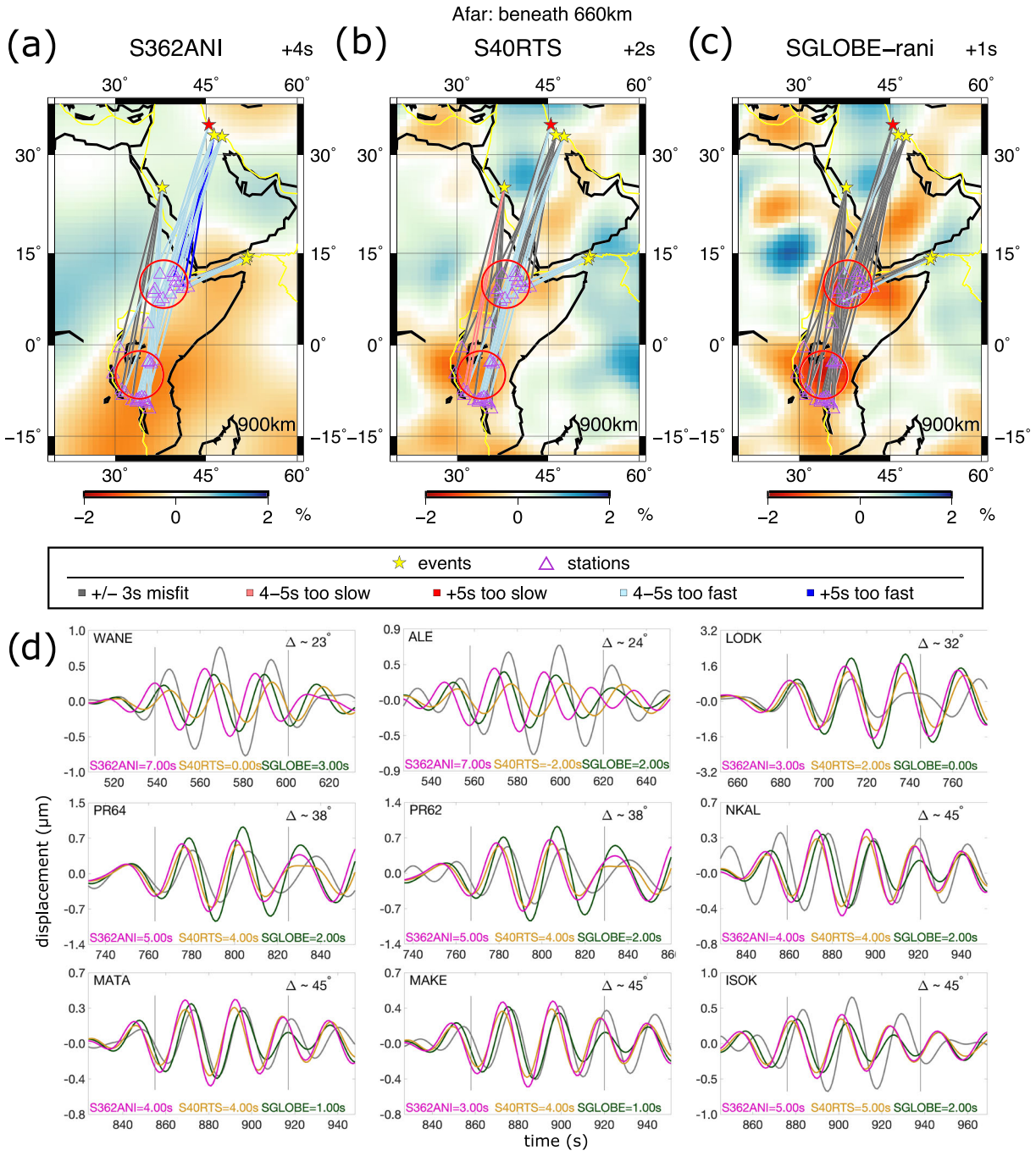

Figure 8. Comparisons of observed and predicted traveltimes and waveforms. Raypaths of direct *S* waves are color coded by the traveltime differences between observed and theoretical waveforms for the global tomography models: (a) S362ANI, (b) S40RTS, and (c) SGLOBE-rani. Red circles indicate the locations of the Afar and the Kenya plumes. (d) Waveform comparisons between observed waveforms (gray) and synthetics from the three models (S362ANI = magenta; S40RTS = orange; SGLOBE-rani = green) for the event corresponding to the red star in (a)–(c).

$$Ra = \frac{\alpha \rho g \Delta T H^3}{\kappa \nu}, \tag{1}$$

where α is thermal expansion coefficient, ρ is density, g is gravity acceleration, ΔT is the temperature difference across the system, H is the thickness of fluid layer, κ is thermal diffusivity, and ν is viscosity. For $Ra > 10^6$ that is typical in mantle, plumes can arise naturally from the bottom of the mantle, and their spacing, size, and duration depend on the vigor of convection (and therefore strongly on mantle

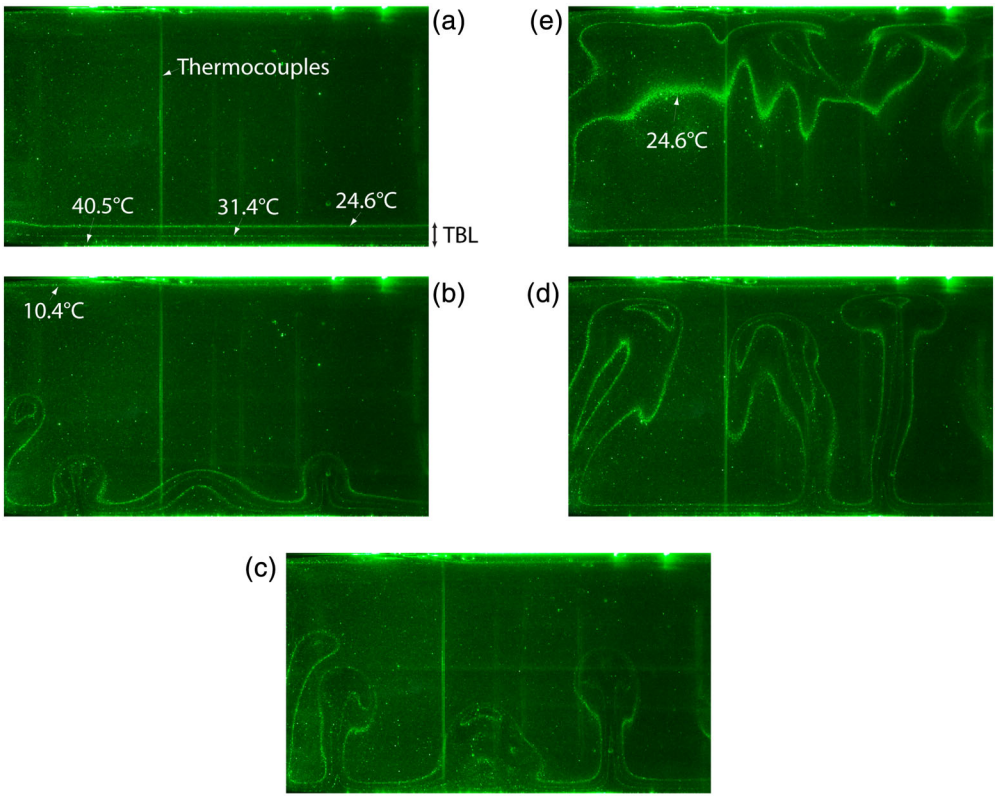

Figure 9. Development of hot, purely thermal plumes in a layer of sugar syrup heated from below and cooled from above at constant temperatures, T_{hot} and T_{cold}, respectively, for a vigor of convection comparable to the mantle's (see Table 2). The bright lines are isotherms, and the images are 30 cm wide. (a) t = 570 s, the isotherms are confined to the lower boundary, delimiting the hot thermal boundary layer (TBL), with a thickness around 1 cm, corresponding to ~100 km in the mantle; (b) t = 820 s, the hot TBL becomes unstable; (c) t = 870 s, plumes rise; (d) t = 970 s, plumes become to spread under the top cold TBL; and (e) t = 1,220 s, all the plumes are spreading under the top cold TBL, and three of them have become disconnected from the bottom hot TBL. Unpublished images from experiment j1m22 of Androvandi et al. (2011).

viscosity) and the presence/absence of compositional heterogeneities. In a compositionally homogeneous mantle, purely thermal plumes would have typical diameters less than 100–300 km and a spacing between 100 and 850 km at the CMB (e.g., Schubert et al., 2004). However, the presence of compositional heterogeneities can change hot plume morphology, with much fatter conduits that can reach 600–1,000 km in diameter (Davaille et al., 2005; Kumagai et al., 2008; Lin & van Keken, 2005) and spacing that can now reach 2,000–3,000 km (Davaille et al., 2005). Given the sizes of LLSVPs, it is therefore expected that several plumes may exist in each LLSVP. Moreover, as illustrated by a laboratory experiment in Figure 9 (corresponding experiment parameters are given in Table 2), plumes are strongly time-dependent features, and they tend to rise vertically because of gravity (Figures 9c and 9d). They spread when they arrive below the lithosphere (Figure 9d) and can even merge there with other nearby plume thermal anomalies (Figure 9e). Individual plumes disappear when they merge or when they have exhausted the hot material from their source thermal boundary layer (Figure 9e). In this case, they first disappear from the bottom up, disconnecting from the bottom hot boundary, so that

Table 2
Laboratory Experiment Parameters Used for Figure 9

T_{cold}	T_{hot}	γ	Ra_{hot}	Ra_{cold}
7.6	48.3	64	1.3×10^6	2.1×10^4

Note. As the viscosity of sugar syrup strongly depends on temperature (as the mantle's), Ra has been calculated using the viscosity at T_{hot} and T_{cold}. γ is the viscosity ratio between the cold and the hot boundaries.

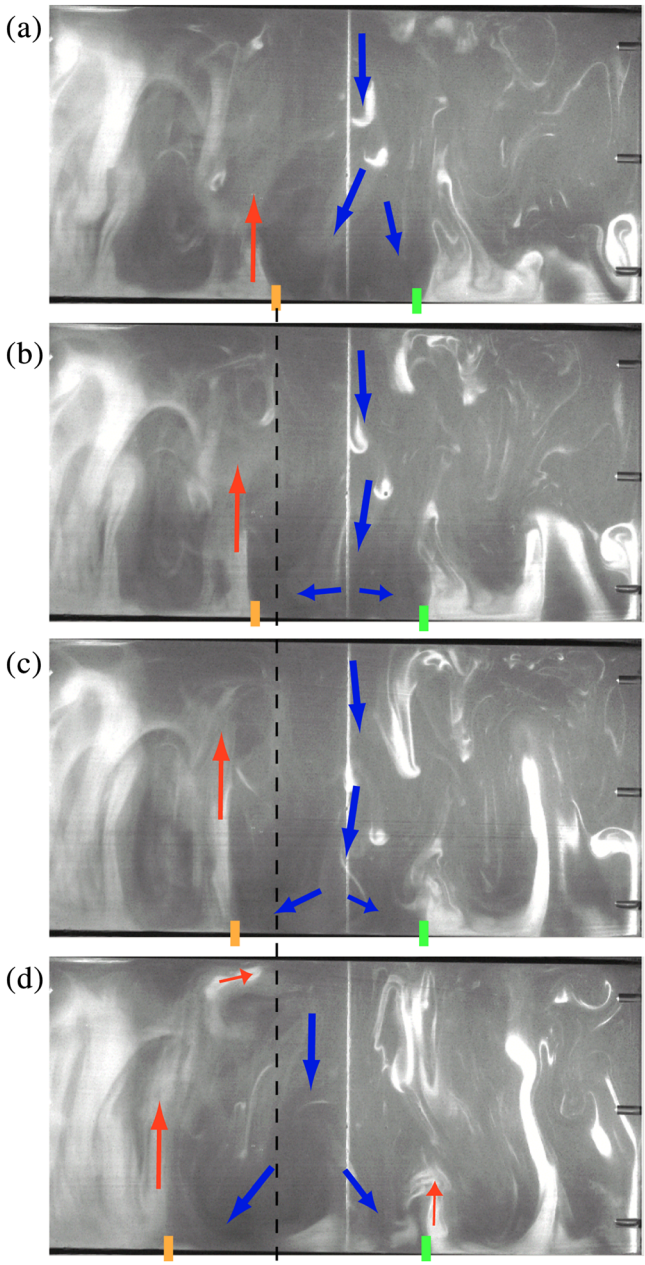

Figure 10. Sequence of images showing the strong influence of a cold downwelling (blue arrows) on plume formation, upwelling (red arrows), and locations (orange and green lines). (a) A cold downwelling (blue arrows) is descending to the bottom, and an upwelling (red arrow) is rising on the left-hand side. (b–d) The cold downwelling is spread at the bottom, and the upwelling on the left-hand side is migrating leftward due to the interaction with the cold downwelling. The images are separated by 30 s. The system was initially composed of two superimposed horizontal layers of fluids with different viscosities, densities, and thicknesses. The lower layer was denser and appeared brighter. The experiment parameters are given in Table 3. Unpublished images from run 18 of Le Bars and Davaille (2004).

their last seismic slow signature will be in the asthenosphere (Figure 9e). If we had only access to the image of Figure 9e, we could be tempted to interpret the continuity of the hot thermal anomaly from the bottom left to the top right as an experimental asthenosphere fed by a unique plume born in the bottom left of the experimental mantle, like Figure 1a and the first interpretation of the early tomographic cross section from South Africa to Afar (Ritsema et al., 1999). However, we see on the sequence of images (Figures 9a–9d) that Figure 9e represents only the last stage of the development of four plumes.

Previous studies have also shown that a plume can become tilted because of plate motion and/or mantle wind (Olson & Singer, 1985; Richards & Griffiths, 1988; Skilbeck & Whitehead, 1978). However, considering thin plume tails (radius ~100 km), Steinberger and Antretter (2006) did not find plume lateral shifts larger than 1,000 km. Moreover, following the analysis by Richards and Griffiths (1988), plate or mantle wind velocity of as fast as 10 cm/yr would not be able to tilt the 400 km radius plumes imaged by tomography by more than a few hundreds of kilometers. In addition, the recent study of Arnould et al. (2020) using 3-D spherical models of mantle convection with self-consistent plate-like behavior also shows the same trend. Simmons et al. (2007) showed that a thermochemical upwelling can account for the tilt of the African superplume using numerical modeling. However, they used traveltime data an order of magnitude less than in the global tomography models considered in this study, which inevitably results in coarse resolution only sufficient for long-wavelength features such as superplume structure. It is therefore impossible to attribute to a single tilted plume the observed thick tomographic structure tilted by 45° between South Africa and Afar. This led Davaille et al. (2005) to interpret the present-day large low-velocity anomaly beneath East Africa as being composed of at least three instabilities in different stages: (i) a large upwelling rising below South Africa, which has not yet reached the upper mantle; (ii) a plume between South Africa and Kenya; and (iii) a dying plume beneath Afar due to the exhaustion of all the material of the thermal boundary layer underneath that region. However, the improved coverage and resolution of the seismic models allow now to refine this view and interpret the present-day tomographic cross sections between South Africa and Afar as the results of ~100 Myr of time-dependent mantle convection.

Another key feature of mantle convection is subducting plates, which constitute the cold downwellings of the convective pattern. Nearby subduction has also been proposed to influence plume formation, duration, and motion (e.g., Androvandi et al., 2011; Becker & Faccenna, 2011; Dannberg & Gassmöller, 2018; Faccenna et al., 2013; Gonnermann et al., 2004; Tan et al., 2002). The spreading of cold subducted slabs onto the CMB will induce horizontal motion in the thermal boundary layer there and confine the hot plume formation region outside of the cold slab area. This behavior is illustrated in a laboratory experiment in Figure 10, and corresponding experiment parameters are given in Table 3. The sequence of images shows how a cold downwelling (outlined with the blue arrows) can strongly influence plume formation (red arrows) and locations (Figure 10). In this experiment, the plumes are thermochemical (in bright color), forming out of a bottom hot and denser layer. We can see the hot upwelling on the left-hand side (orange bar) migrates leftward because of the interaction with the cold downwelling. From a tomographic point of view, the hot plume formation region could be

Table 3
Laboratory Experiment Parameters Used for Figure 10

a	γ	Ra	B
0.30	21	8.8×10^6	0.31

Note. a is the initial thickness ratio (bottom/top); γ is the viscosity ratio; Ra was calculated with the viscosity of the bottom layer; and B is the buoyancy ratio, which compares the density contrast between the two layers of compositional origin with the density contrast of thermal origin. More details on the experimental procedure can be found in Le Bars and Davaille (2004).

assimilated with an LLSVP. The nearby subduction of the Tethyan slab (Figure 3) is therefore a good candidate to induce lateral motion above the CMB that could potentially lead to substantial deflections of mantle plumes in the region. The Tethyan slab has been subducting to the lowermost mantle since the late Jurassic (~150 Ma; Van der Voo et al., 1999), and its seismic signature has been reported by several studies. For example, Rao et al. (2017) found substantial anisotropy in the lowermost mantle beneath the Indian Ocean from ScS splitting measurements, which they attributed to lattice preferred orientation deformation of the Tethyan subducted slab dipping southwestwardly. This geometry is consistent with the migration of the subducted Tethyan slab toward the African LLSVP with time, which in turn may have pushed the LLSVP westward. Furthermore, Lynner and Long (2014) identified strong deformation just outside the boundary of the African LLSVP beneath Afar using shear wave splitting data from SK(K)S phases, which also indicates the interaction between the subducted Tethyan slab and the African LLSVP. According to a recent plate reconstruction study by Young et al. (2019), the eastern boundary of the African LLSVP has moved westward due to an interaction with Tethyan slab at an average speed of ~1.3 cm/yr since 130 Ma, which may have caused ~400 km westward drift on the CMB during the last 30 Myr since the massive eruption in Afar. Therefore, it is very plausible that the boundary of the African LLSVP at the CMB enclosed the region beneath Afar more than 30 Ma, providing a deep mantle source for the plume. Hence, it can explain the present-day lack of slow anomaly in the deep lower mantle underneath Afar, but it could certainly not have pushed the source of Afar all the way down to beneath South Africa.

6. Discussion

6.1. Three Plume Scenario and Dying Afar Plume

The geochemical and geophysical differences between the Ethiopian and the Kenyan plateaux presented in sections 2 and 3 are not compatible with the two plume model with distinct sources at the CMB (e.g., Pik et al., 2006; Rogers et al., 2000; Figure 1b) nor with the African superplume model (e.g., Hansen et al., 2012; Ritsema et al., 1999; Figure 1a). Moreover, two distinct plume heads in the upper mantle and the uppermost lower mantle beneath Afar and Kenya are observed in recent global tomography models, which are supported by independent seismological tests (section 4) and geodynamic laboratory experiments (section 5).

However, there are a few questions still to be answered. The first one is how the two distinct plume heads can originate from a common source at the CMB but lead to no hotspot track of the Afar plume, unlike its counterpart, the Kenya plume. According to a paleomagnetic reconstruction study by Vicente de Gouveia et al. (2018), a plume under Afar right now cannot have produced the Ethiopian-Yemen traps ~30 Ma, because Africa has moved ~1,000 km toward the northeast since then. Hence, they proposed the existence of three plumes in the region—the Afar and the Kenya plumes, which were discussed previously in this study, plus the so-called East Africa plume (hereafter we call it the Ethiopia plume since it generated the Ethiopia-Yemen traps), which impinged beneath Ethiopia about 30 Ma. They suggested that an associated massive volcanic eruption led to the Ethiopia-Yemen traps ~30 Ma, which may have exhausted the Ethiopia plume's material. This seems to be consistent with recent global tomography models (Figures 5 and 6) showing weak low-velocity anomalies in the upper mantle region of the Ethiopia plume currently (located at 6°N, 34°E according to Vicente de Gouveia et al., 2018, and hereafter referred to as "X_E").

In practice, the Ethiopia plume may be impossible to detect in global tomography models due to their limited resolution. In order to better investigate the presence of the Ethiopia plume, in Figure 11, we present depth slices of two recent high-resolution regional waveform tomography models for the upper mantle, Emry et al.'s (2019) model and AF2019 (Celli et al., 2020). Since these regional tomographic models are built using more data from Africa such as AfricaArray than global models, their resolution (~5°) seems to be around twice better than those of typical global models (~10°) as shown in their resolution tests. We observe that these regional models both show a third low-velocity anomaly at 400–500 km depth in addition to anomalies corresponding to the Afar and the Kenya plumes, which is also observed in other regional tomography models using teleseismic traveltime data (Bastow et al., 2008; Civiero et al., 2015, 2016). The exact

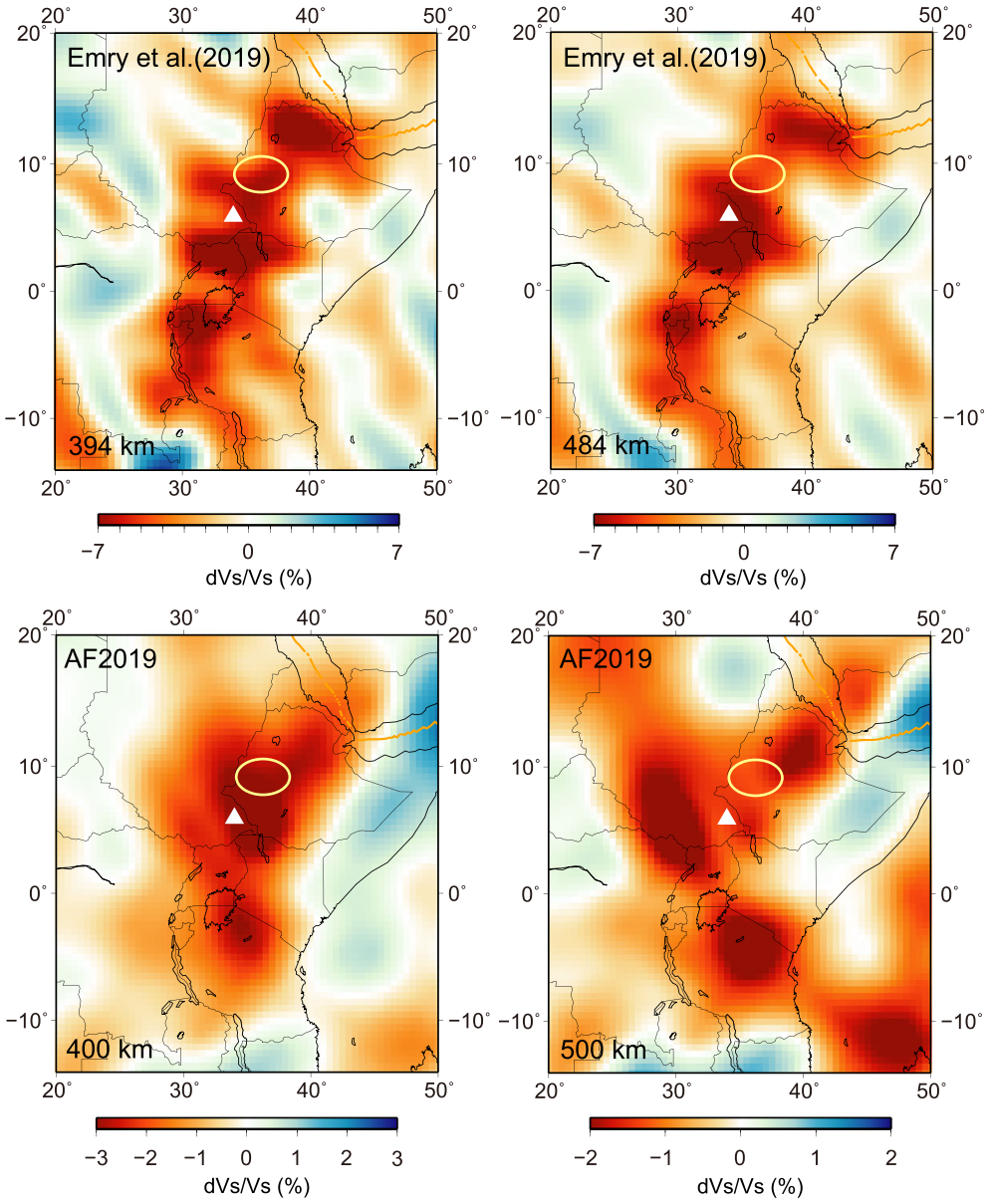

Figure 11. Depth slices of the regional models by Emry et al. (2019) and Celli et al. (2020; AF2019) at ~400–500 km. Yellow ellipses indicate locations of low-velocity anomalies other than those corresponding to the Afar and the Kenya plumes observed in other regional tomography models (Bastow et al., 2008; Civiero et al., 2015, 2016). White triangles represent the position of "the East Africa plume" suggested by Vicente de Gouveia et al. (2018).

location of this third low-velocity anomaly varies from model to model. AF2019 (Celli et al., 2020) shows a low-velocity anomaly west of X_E at 500 km depth but directly beneath it at 400 km depth, while the anomaly in Emry et al.'s (2019) model is rightly beneath X_E at ~400–500 km depth. Therefore, we may be able to interpret this low-velocity anomaly as the Ethiopia plume. Otherwise, it could be a secondary plume diverging from the Afar plume. It is noteworthy that the two waveform tomography models show that the Ethiopia plume merges with the Afar plume at shallow depths (see Figures 4 and 11). The mixing of the Ethiopia plume with the Afar plume further highlights why global tomography models can hardly distinguish the two plumes. In conclusion, the Afar plume has risen with an origin ~600 km east of the Ethiopia plume at the CMB (Vicente de Gouveia et al., 2018), and it may have become a dying plume because its plume tail was disconnected from the CMB by the interaction between the westward migrating Tethyan slab and the African LLSVP as discussed in section 5. The chronology of the Ethiopia and the Afar plumes is

also compatible with the observation of the highest temperatures from old and recent basalts in roughly the same place in the Ethiopian plateau discussed in section 2. The highest mantle temperature beneath Afar may have been caused by the Ethiopia plume at 40–10 Ma, but since 10 Ma, it is mainly due to the Afar plume.

The second question is why there is a strong low-velocity anomaly in the uppermost lower mantle beneath Afar (ellipses in Figure 3). The rising of the plume is likely hampered at the 660 km discontinuity due to the negative Clapeyron slope of the postspinel phase transition, which implies that the thermal buoyancy of the plume is weak, leading to an accumulation of plume-tail material in the uppermost lower mantle. If the temperature of the Afar plume was higher than 1800°C at 660 km depth, the positive Clapeyron slope of the majorite-bridgmanite transition would dominate, expediting the upwelling speed of the Afar plume, because the depth range of stable majorite greatly expands at high temperatures (Hirose, 2002). Therefore, the low-velocity anomaly observed beneath the 660 km discontinuity suggests that the Afar plume is currently not very hot and has weak buoyancy, which is consistent with the view of the Afar plume being a dying plume. Furthermore, compositional heterogeneity may be partly responsible for the strong low-velocity anomaly in the uppermost lower mantle between the postspinel phase transition (~660 km) and postgarnet phase transition (~1,000 km). Basalt has lower density for this depth range than pyrolite but higher density for the depth ranges above and below (e.g., Faccenda & Dal Zilio, 2017). Jenkins et al. (2017) suggested compositional variations (maybe due to basalts) in areas of mantle upwelling in the midmantle beneath Europe and North Atlantic based on a sharp boundary at ~1,000 km depth from receiver functions. Ballmer et al. (2015) also suggested compositional heterogeneity could pond around this depth due to a neutral buoyancy crossover for basaltic material. Therefore, the strong low-velocity anomaly may indicate that a large fraction of basalt component from recycled oceanic crust may be stabilized in this depth range as in the case of stagnant slabs (Ballmer et al., 2015), not implying a strong thermal anomaly.

There is another line of evidence supporting the absence of a strong thermal anomaly in the upper mantle beneath Afar. The normal MTZ thickness found beneath Afar by receiver function studies (Reed et al., 2016; Thompson et al., 2015) may imply the presence of a weak thermal anomaly. Furthermore, the MTZ beneath Afar is believed to be hydrated according to receiver function studies (cyan lines in Figures 3a–3c and 3g–3i) as suggested by reports of a melt layer atop the 410 km discontinuity beneath the region (Tauzin et al., 2010; Thompson et al., 2015) and a prominent 520 km discontinuity (Thompson et al., 2015), which may be caused by the shrinkage of the loop width of wadsleyite and ringwoodite in hydrous conditions (Inoue et al., 2010). The mantle temperatures beneath Afar proposed by Rooney, Herzberg, and Bastow (2012) and Ferguson et al. (2013) are within 1370–1490°C, which is close to the lower end for the temperature range of large igneous provinces (Rooney, Herzberg, & Bastow, 2012). Therefore, the strong low-velocity anomaly in the upper mantle beneath Afar cannot be attributed to a thermal anomaly alone, requiring other sources such as H_2O and CO_2-related melt, which may be linked to the hydrous MTZ and basaltic composition of the Afar plume. Rychert et al. (2012) found a strong velocity increase at ~75 km depth beneath Afar using *S*-to-*P* receiver functions and used geodynamical modeling to interpret it as decompression melting in the absence of a strong thermal anomaly. These studies support that a strong thermal anomaly is absent in the upper mantle beneath Afar, which leads to the conclusion that the Afar plume may be losing its heat, detached from the CMB.

6.2. Evolution of Mantle Plumes in East Africa

Putting together the range of multidisciplinary information assembled in this study, we conclude that there are currently two active plumes beneath East Africa. While the Afar plume is likely to have a common source with the Kenya plume in the African LLSVP, the two plumes have been upwelling separately. The Afar plume is now detached from the African LLSVP possibly due to the interaction with the subducted Tethyan slab, and as a consequence, it is dying out. However, as paleomagnetic reconstructions show that the current Afar plume cannot be responsible for the Ethiopia-Yemen traps formed ~30 Ma, the traps must have been created by a third "Ethiopia" plume (Vicente de Gouveia et al., 2018) that has been subsequently getting mixed with the Afar plume. This time-dependent three-plume scenario explains well the geochemical observations of no hotspot track of the Afar plume unlike its counterpart in the Kenyan plateau and a third low-velocity anomaly in the upper mantle between the Afar and the Kenya plumes in recent regional tomography models (Celli et al., 2020; Emry et al., 2019).

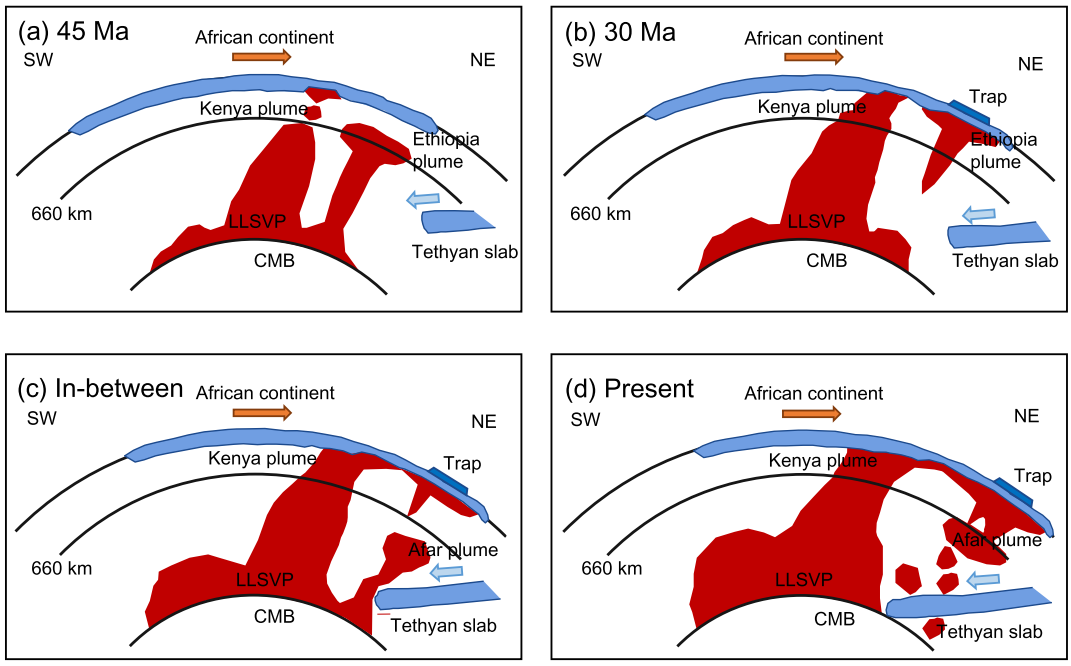

Figure 12. Cartoon summarizing the evolution of the Kenya, the Ethiopia, and the Afar plumes proposed in this study. (a) The Kenya plume erupted in Turkana on an episodic basis since 45 Ma (Ebinger et al., 1993). An orange arrow indicates the direction of the African plate motion. (b) The Ethiopia plume erupted a massive flood basalt around 30 Ma, leading to the emplacement of the Ethiopia-Yemen traps (Hofmann et al., 1997). (c) The Afar plume rises, and the subducted Tethyan slab interacts with the African LLSVP, leading to the cutoff of the Afar plume from the LLSVP. (d) The Afar plume tail has accumulated beneath the 660 km discontinuity, losing its heat, and the Ethiopia plume is merging with the Afar plume currently.

Based on the geochemical and geophysical observations we have listed so far, Figure 12 summarizes the alternative mechanism that we propose for the evolution of mantle plumes in East Africa. Three major plumes originated from the same source near the CMB at different times—the Kenya, the Ethiopia, and the Afar plumes. While the Kenya plume impinged beneath Turkana on an episodic basis 45 Ma (Figure 12a), the Ethiopia plume caused a massive flood basalt ~30 Ma (Figure 12b). It is still unclear why eruption styles are different for the Kenya and Ethiopia plumes. It could be related to compositional variations in the Kenya plume (Nelson et al., 2012) or the presence of the Tanzanian craton and its interaction with the Kenya plume, which led to the mixing of subcontinental lithospheric mantle and plume material (Halldórsson et al., 2014). Meanwhile, when the Afar plume was rising, the subducted Tethyan slab reached the CMB, pushing the African LLSVP and the base of the Afar plume westward (Figure 12c). This led to a cutoff of the Afar plume from the LLSVP, so that the Afar plume lost its source and started to progressively cool down. The not-very-hot plume tail ascending after the cutoff has accumulated beneath the 660 km discontinuity as shown in recent tomography models due to the negative Clapeyron slope at the postspinel phase transition and the possible compositional heterogeneity in the Afar plume (Figure 12d). With this alternative interpretation, we can successfully explain all the available geochemical and geophysical observations of the region (different chemical compositions, timing, eruption styles, and hotspot track patterns in the basalts in East Africa from geochemical observations; different plume morphology beneath Kenya and Afar, a third low-velocity anomaly between the Kenya and the Afar plumes, and a strong low-velocity anomaly just beneath the 660 km discontinuity beneath Afar from geophysical observations), which cannot be explained with a single, strongly tilted, large plume model.

7. Conclusions

Mantle plumes in East Africa show many unique geochemical and geophysical features. In order to explain the wide range of observations available, we propose an alternative interpretation of the evolution of

upwellings in the region suggesting that there exist at least two separate Afar and Kenya plumes that share the same deep mantle source near the CMB but rise separately, and a third Ethiopia mantle plume existed leading to the Ethiopia-Yemen traps ~30 Ma. The Afar plume seems to be currently a dying plume, which is consistent with (i) the lack of low-velocity anomalies beneath Afar below ~1,000 km depth in recent global tomography models, (ii) a strong low-velocity anomaly just beneath the 660 km discontinuity beneath Afar interpreted as accumulation of plume-tail material, (iii) relatively low mantle potential temperature beneath Afar comparing to large igneous provinces (Rooney, Herzberg, & Bastow, 2012), and (iv) decompression melting at ~75 km that indicates the absence of a strong thermal anomaly (Rychert et al., 2012). We perform waveform modeling and geodynamic laboratory experiments that support this interpretation.

The cutoff of the Afar plume from the base of the mantle is probably due to the interaction between the subducted Tethyan slab and the African LLSVP, which highlights that mantle plumes can evolve in complex ways through time. Because of a lack of magmatic supply from such dying, cooling Afar plume, the continental breakup along the Main Ethiopian Rift would fail in the near future, not leading to the stage of seafloor spreading. This is a new suggestion, and it will be interesting to see if future studies support this idea. Thus, our understanding of the evolution of mantle plumes may shed new light on the connection between LLSVPs and surface plate tectonics and, consequently, on the evolution of life in this habitable planet.

Data Availability Statement

Tomography models used in this paper are available from IRIS Data Services Products (http://ds.iris.edu/ds/products/emc-earthmodels/). AF2019 model can be found in the author's website (https://nlscelli.wixsite.com/ncseismology/af2019). The Generic Mapping Tools software (Wessel et al., 2013) was used to plot figures containing maps.

Acknowledgments

This research was supported by the National Research Foundation of Korea (NRF) grant funded by the Korean government (MSIT) (2019R1A2C208506111), by the Korea Meteorological Administration Research and Development Program under Grant KMI2018-09312, by Basic Science Research Program through the National Research Foundation of Korea (NRF) funded by the Ministry of Education (2019R1A6A1A03033167), and by a research grant of Kangwon National University in 2019. A. M. G. F. thanks support from Natural Environment Research Council (NERC) projects NE/K005669/1 and NE/N011791/1. We acknowledge the availability of global seismograms used in section 4.3 from the Data Management Center of IRIS (http://www.iris.edu/ds/nodes/dmc/), and details about the seismic networks are given in Table S1.

References

Amit, H., & Olson, P. (2015). Lower mantle superplume growth excites geomagnetic reversals. *Earth and Planetary Science Letters*, *414*, 68–76. https://doi.org/10.1016/j.epsl.2015.01.013

Androvandi, S., Davaille, A., Limare, A., Fouquier, A., & Marais, C. (2011). At least three scales of convection in a mantle with strongly temperature-dependent viscosity. *Physics of the Earth and Planetary Interiors*, *188*, 132–141. https://doi.org/10.1016/j.pepi.2011.07.004

Arnould, M., Coltice, N., Flament, N., & Mallard, C. (2020). Plate tectonics and mantle control on plume dynamics. *Earth and Planetary Science Letters*. https://doi.org/10/1016/j.epsl.2020.116439

Auer, L., Boschi, L., Becker, T. W., Nissen-Meyer, T., & Giardini, D. (2014). Savani: A variable resolution whole-mantle model of anisotropic shear velocity variations based on multiple data sets. *Journal of Geophysical Research: Solid Earth*, *119*, 3006–3034. https://doi.org/10.1002/2013JB010773

Backus, G. E., & Gilbert, J. F. (1968). The resolving power of gross Earth data. *Geophysical Journal of the Royal Astronomical Society*, *16*, 169–205. https://doi.org/10.1111/j.1365-246x.1968.tb00216.x

Ballmer, M., Schmerr, N. C., Nakagawa, T., & Ritsema, J. (2015). Compositional mantle layering revealed by slab stagnation at ~1000-km depth. *Science Advances*, *1*(11), e1500815. https://doi.org/10.1126/sciadv.1500815

Bassin, C., Laske, G., & Masters, G. (2000). *The current limits of resolution for surface wave tomography in North America* (Vol. 81). Washington, DC: Eos Trans. AGU.

Bastow, I. D., Nyblade, A. A., Stuart, G. W., Rooney, T. O., & Benoit, M. H. (2008). Upper mantle seismic structure beneath the Ethiopean hot spot: Rifting at the edge of the African low-velocity anomaly. *Geochemistry, Geophysics, Geosystems*, *9*, Q12022. https://doi.org/10.1029/2008GC002107

Becker, T. W., & Faccenna, C. (2011). Mantle conveyor beneath the Tethyan collisional belt. *Earth and Planetary Science Letters*, *310*(3–4), 453–461. https://doi.org/10.1016/j.epsl.2011.08.021

Benoit, M. H., Nyblade, A. A., Owens, T. J., & Stuart, G. (2006). Mantle transition zone structure and upper mantle S velocity variations beneath Ethiopia: Evidence for a broad, deep-seated thermal anomaly. *Geochemistry, Geophysics, Geosystems*, *7*, Q11013. https://doi.org/10.1029/2006GC001398

Benoit, M. H., Nyblade, A. A., & VanDecar, J. C. (2006). Upper mantle P-wave speed variations beneath Ethiopia and the origin of the Afar hotspot. *Geology*, *34*, 329–332. https://doi.org/10.1130/g22281.1

Burke, K., Steinberger, B., Torsvik, T. H., & Smethurst, M. A. (2008). Plume generation zones at the margins of large low shear velocity provinces on the core-mantle boundary. *Earth and Planetary Science Letters*, *265*, 49–60. https://doi.org/10.1016/j.epsl.2007.09.042

Celli, N. L., Lebedev, S., Schaeffer, A. J., & Gaina, C. (2020). African cratonic lithosphere carved by mantle plumes. *Nature Communications*, *11*(1), 92. https://doi.org/10.1038/s41467-019-13871-2

Chang, S.-J., & Ferreira, A. M. G. (2019). Inference on water content in the mantle transition zone near subducted slabs from anisotropy tomography. *Geochemistry, Geophysics, Geosystems*, *20*, 1189–1201. https://doi.org/10.1029/2018GC008090

Chang, S.-J., Ferreira, A. M. G., Ritsema, J., van Heijst, H. J., & Woodhouse, J. H. (2014). Global radially anisotropic mantle structure from multiple datasets: A review, current challenges, and outlook. *Tectonophysics*, *617*, 1–19. https://doi.org/10.1016/j.tecto.2014.01.033

Chang, S.-J., Ferreira, A. M. G., Ritsema, J., van Heijst, H. J., & Woodhouse, J. H. (2015). Joint inversion for global isotropic and radially anisotropic mantle structure including crustal thickness perturbations. *Journal of Geophysical Research: Solid Earth*, *120*, 4278–4300. https://doi.org/10.1002/2014JB011824

Chang, S.-J., & van der Lee, S. (2011). Mantle plumes and associated flow beneath Arabia and East Africa. *Earth and Planetary Science Letters*, *302*, 448–454. https://doi.org/10.1016/j.epsl.2010.12.050

Civiero, C., Goes, S., Hammond, J. O. S., Fishwick, S., Ahmed, A., Ayele, A., et al. (2016). Small-scale thermal upwellings under the northern East African Rift from S travel time tomography. *Journal of Geophysical Research: Solid Earth*, *121*, 7395–7408. https://doi.org/10.1002/2016JB013070

Civiero, C., Hammond, J. O. S., Goes, S., Fishwick, S., Ahmed, A., Ayele, A., et al. (2015). Multiple mantle upwellings in the transition zone beneath the northern East-African Rift system from relative P-wave travel-time tomography. *Geochemistry, Geophysics, Geosystems*, *16*, 2949–2968. https://doi.org/10.1002/2015GC005948

Courtillot, V., & Olson, P. (2007). Mantle plumes link magnetic superchrons to Phanerozoic mass depletion events. *Earth and Planetary Science Letters*, *260*, 495–504. https://doi.org/10.1016/j.epsl.2007.06.003

Dannberg, J., & Gassmöller, R. (2018). Chemical trends in ocean islands explained by plume-slab interaction. *Proceedings of the National Academy of Sciences*, *115*, 4351–4356. https://doi.org/10.1073/pnas.1714125115

Daradich, A., Mitrovica, J. X., Pysklywec, R. N., Willett, S. D., & Forte, A. M. (2003). Mantle flow, dynamic topography, and rift-flank uplift of Arabia. *Geology*, *31*, 901–904. https://doi.org/10.1130/g19661.1

Davaille, A., & Limare, A. (2015). Laboratory studies of mantle convection. In D. Bercovici & J. Schubert (Eds.), *Treatise of geophysics*, *Mantle Dynamics* (2nd ed., Vol. 7, pp. 73–144). Amsterdam: Elsevier.

Davaille, A., Stutzmann, E., Silveira, G., Besse, J., & Courtillot, V. (2005). Convective patterns under the Indo-Atlantic box. *Earth and Planetary Science Letters*, *239*, 233–252. https://doi.org/10.1016/j.epsl.2005.07.024

Durand, S., Debayle, E., Ricard, Y., Zaroli, C., & Lambotte, S. (2017). Confirmation of a change in the global shear velocity pattern at around 1000 km depth. *Geophysical Journal International*, *211*, 1628–1639. https://doi.org/10.1093/gji/ggx405

Ebinger, C. J., & Sleep, N. H. (1998). Cenozoic magmatism throughout East Africa resulting from impact of a single plume. *Nature*, *395*, 788–791. https://doi.org/10.1038/27417

Ebinger, C. J., Yemane, T., Woldegabriel, G., Aronson, J. L., & Walter, R. C. (1993). Late Eocene-recent volcanism and faulting in the southern main Ethiopian rift. *Journal of the Geological Society, London*, *150*, 99–108. https://doi.org/10.1144/gsjgs.150.1.0099

Emry, E. L., Shen, Y., Nyblade, A. A., Flinders, A., & Bao, X. (2019). Upper mantle Earth structure in Africa from full-wave ambient noise tomography. *Geochemistry, Geophysics, Geosystems*, *20*, 120–147. https://doi.org/10.1029/2018GC007804

Faccenna, C., Becker, T. W., Conrad, C. P., & Husson, L. (2013). Mountain building and mantle dynamics. *Tectonics*, *32*, 80–93. https://doi.org/10.1029/2012TC003176

Faccenda, M., & Dal Zilio, L. (2017). The role of solid-solid phase transitions in mantle convection. *Lithos*, *268–271*, 198–224. https://doi.org/10.1016/j.lithos.2016.11.007

Ferguson, D. J., Maclennan, J., Bastow, I. D., Pyle, D. M., Jones, S. M., Keir, D., et al. (2013). Melting during late-stage rifting in Afar is hot and deep. *Nature*, *499*(7456), 70–73. https://doi.org/10.1038/nature12292

Ferreira, A. M. G., Faccenda, M., Sturgeon, W., Chang, S.-J., & Schardong, L. (2019). Ubiquitous lower-mantle anisotropy beneath subduction zones. *Nature Geoscience*, *12*, 301–306. https://doi.org/10.1038/s41561-019-0325-7

French, S. W., & Romanowicz, B. (2014). Whole-mantle radially anisotropic shear velocity structure from spectral-element waveform tomography. *Geophysical Journal International*, *199*, 1303–1327. https://doi.org/10.1093/gji/ggu334

Furman, T., Kaleta, K. M., Bryce, J. G., & Hanan, B. B. (2006). Tertiary mafic lavas of Turkana, Kenya: Constraints on East African plume structure and the occurrence of high-μ volcanism in Africa. *Journal of Petrology*, *47*, 1221–1244. https://doi.org/10.1093/petrology/egl009

Garnero, E. J., & McNamara, A. K. (2008). Structure and dynamics of Earth's lower mantle. *Science*, *320*(5876), 626–628. https://doi.org/10.1126/science.1148028

George, R., Rogers, N., & Kelley, S. (1998). Earliest magmatism in Ethiopia: Evidence for two mantle plumes in one flood basalt province. *Geology*, *26*, 923–926. https://doi.org/10.1130/0091-7613(1998)026<0923:emieef>2.3.co;2

Goes, S., Cammarano, F., & Hansen, U. (2004). Synthetic seismic signature of thermal mantle plumes. *Earth and Planetary Science Letters*, *218*, 403–419. https://doi.org/10.1016/s0012-821x(03)00680-0

Gonnermann, H. M., Jellinek, A. M., Richards, M. A., & Manga, M. (2004). Modulation of mantle plumes and heat flow at the core mantle boundary by plate-scale flow: Results from laboratory experiments. *Earth and Planetary Science Letters*, *226*, 53–67. https://doi.org/10.1016/j.epsl.2004.07.021

Halldórsson, S. A., Hilton, D. R., Scarsi, P., Abebe, T., & Hopp, J. (2014). A common mantle plume source beneath the entire East African Rift system revealed by coupled helium-neon systematics. *Geophysical Research Letters*, *41*, 2304–2311. https://doi.org/10.1002/2014GL059424

Hansen, S. E., & Nyblade, A. A. (2013). The deep seismic structure of the Ethiopia/Afar hotspot and the African superplume. *Geophysical Journal International*, *194*, 118–124. https://doi.org/10.1093/gji/ggt116

Hansen, S. E., Nyblade, A. A., & Benoit, M. H. (2012). Mantle structure beneath Africa and Arabia from adaptively parameterized P-wave tomography: Implications for the origin of Cenozoic Afro-Arabian tectonism. *Earth and Planetary Science Letters*, *319–320*, 23–34. https://doi.org/10.1016/j.epsl.2011.12.023

Hilton, D. R., Halldórsson, S. A., Barry, P. H., Fischer, T. P., de Moor, J. M., Ramirez, C. J., et al. (2011). Helium isotopes at Rungwe Volcanic Province, Tanzania, and the origin of East African Plateaux. *Geophysical Research Letters*, *38*, L21304. https://doi.org/10.1029/2011GL049589

Hirose, K. (2002). Phase transitions in pyrolitic mantle around 670-km depth: Implications for upwelling of plumes from the lower mantle. *Journal of Geophysical Research*, *107*. https://doi.org/10.1029/2001JB000597

Hofmann, C., Courtillot, V., Féraud, G., Rochette, P., Yirgu, G., Ketefo, E., & Pik, R. (1997). Timing of the Ethiopian flood basalt event and implications for plume birth and global change. *Nature*, *389*, 838–841. https://doi.org/10.1038/39853

Inoue, T., Wada, T., Sasaki, R., & Yurimoto, H. (2010). Water partitioning in the Earth's mantle. *Physics of the Earth and Planetary Interiors*, *183*, 245–251. https://doi.org/10.1016/j.pepi.2010.08.003

Jenkins, J., Deuss, A., & Cottaar, S. (2017). Converted phases from sharp 1000 km depth mid-mantle heterogeneity beneath Western Europe. *Earth and Planetary Science Letters*, *459*, 196–207. https://doi.org/10.1016/j.epsl.2016.11.031

Komatitsch, D., & Tromp, J. (2002a). Spectral-element simulations of global seismic wave propagation—I. Validation. *Geophysical Journal International*, *149*, 390–412. https://doi.org/10.1046/j.1365-246x.2002.01653.x

Komatitsch, D., & Tromp, J. (2002b). Spectral-element simulations of global seismic wave propagation—II. Three-dimensional models, oceans, rotation and self-gravitation. *Geophysical Journal International*, *150*, 303–318. https://doi.org/10.1046/j.1365-246x.2002.01716.x

Kumagai, I., Davaille, A., Kurita, K., & Stutzmann, E. (2008). Mantle plumes: Thin, fat, successful, or failing? Constraints to explain hot spot volcanism through time and space. *Geophysical Research Letters*, *35*, L16301. https://doi.org/10.1029/2008GL035079

Kustowski, B., Ekström, G., & Dziewoński, A. M. (2008). Anisotropic shear-wave velocity structure of the Earth's mantle: A global model. *Journal of Geophysical Research*, *113*, B06306. https://doi.org/10.1029/2007JB005169

Le Bars, M., & Davaille, A. (2004). Whole layer convection in a heterogeneous planetary mantle. *Journal of Geophysical Research*, *109*, B03403. https://doi.org/10.1029/2003JB002617

Lekic, V., Cottaar, S., Dziewonski, A., & Romanowicz, B. (2012). Cluster analysis of global lower mantle tomography: A new class of structure and implications for chemical heterogeneity. *Earth and Planetary Science Letters*, *357–358*, 68–77. https://doi.org/10.1016/j.epsl.2012.09.014

Li, Z.-X., & Zhong, S. (2009). Supercontinent-superplume coupling, true polar wander and plume mobility: Plate dominance in whole-mantle tectonics. *Physics of the Earth and Planetary Interiors*, *176*, 143–156. https://doi.org/10.1016/j.pepi.2009.05.004

Lin, S.-C., Kuo, B.-Y., Chiao, L.-Y., & van Keken, P. E. (2005). Thermal plume models and melt generation in East Africa: A dynamic modeling approach. *Earth and Planetary Science Letters*, *237*, 175–192. https://doi.org/10.1016/j.epsl.2005.04.049

Lin, S.-C., & van Keken, P. (2005). Multiple volcanic episodes of flood basalts caused by thermochemical mantle plumes. *Nature*, *436*(7048), 250–252. https://doi.org/10.1038/nature03697

Lithgow-Bertelloni, C., & Silver, P. G. (1998). Dynamic topography, plate driving forces and the African superswell. *Nature*, *395*, 269–272. https://doi.org/10.1038/26212

Locke, J. A., Bryce, J. G., Furman, T., Hanan, B. B., Rooney, T., & Graham, D. G. (2008). Hf isotopic insights into mantle source contributions in Turkana, East African Rift system. *Geochimica et Cosmochimica Acta*, *72*, A566. https://doi.org/10.1016/j.gca.2016.03.024

Lynner, C., & Long, M. D. (2014). Lowermost mantle anisotropy and deformation along the boundary of the African LLSVP. *Geophysical Research Letters*, *41*, 3447–3454. https://doi.org/10.1002/2014GL059875

MacQueen, J. (1967). Some methods for classification and analysis of multivariate observations. In L. M. le Cam & J. Neyman (Eds.), *Proceedings of the Fifth Berkeley Symposium on Mathematical Statistics and Probability* (Vol. 1, pp. 281–297). Berkeley: University of California Press.

Maguire, R., Ritsema, J., Bonnin, M., van Keken, P. E., & Goes, S. (2018). Evaluating the resolution of deep mantle plumes in teleseismic traveltime tomography. *Journal of Geophysical Research: Solid Earth*, *123*, 384–400. https://doi.org/10.1002/2017JB014730

Maguire, R., Ritsema, J., van Keken, P. E., Fichtner, A., & Goes, S. (2016). *P*- and *S*-wave delays caused by thermal plumes. *Geophysical Journal International*, *206*, 1169–1178. https://doi.org/10.1093/gji/ggw187

Marty, B., Pik, R., & Gezahegn, Y. (1996). Helium isotopic variations in Ethiopian plume lavas: Nature of magmatic sources and limit on lower mantle contribution. *Earth and Planetary Science Letters*, *144*, 223–237. https://doi.org/10.1016/0012-821x(96)00158-6

Montelli, R., Nolet, G., Dahlen, F. A., & Masters, G. (2006). A catalogue of deep mantle plumes: New results from finite-frequency tomography. *Geochemistry, Geophysics, Geosytems*, *7*, Q11007. https://doi.org/10.1029/2006GC001248

Montelli, R., Nolet, G., Dahlen, F. A., Masters, G., Engdahl, E. R., & Hung, S.-H. (2004). Finite-frequency tomography reveals a variety of plumes in the mantle. *Science*, *303*(5656), 338–343. https://doi.org/10.1126/science.1092485

Moucha, R., & Forte, A. M. (2011). Changes in African topography driven by mantle convection. *Nature Geoscience*, *4*, 707–712. https://doi.org/10.1038/ngeo1235

Mulibo, G. D., & Nyblade, A. A. (2013). Mantle transition zone thinning beneath eastern Africa: Evidence for a whole-mantle superplume structure. *Geophysical Research Letters*, *40*, 1–5. https://doi.org/10.1002/grl.50694

Nelson, W. R., Furman, T., van Keken, P. E., Shirey, S. B., & Hanan, B. B. (2012). Os-Hf isotopic insight into mantle plume dynamics beneath the East African Rift system. *Chemical Geology*, *320–321*, 66–79. https://doi.org/10.1016/j.chemgeo.2012.05.020

Nyblade, A. A., Durrheim, R., Dirks, P., Graham, G., Gibson, R., & Webb, S. (2011). Geoscience initiative develops sustainable science in Africa. *Eos*, *92*(19), 161–162. https://doi.org/10.1029/2011eo190002

Olson, P., & Singer, H. (1985). Creeping plumes. *Journal of Fluid Mechanics*, *158*, 511–531. https://doi.org/10.1017/s0022112085002749

Pik, R., Marty, B., & Hilton, D. R. (2006). How many mantle plumes in Africa? The geochemical point of view. *Chemical Geology*, *226*, 100–114. https://doi.org/10.1016/j.chemgeo.2005.09.016

Rao, B. P., Kumar, M. R., & Singh, A. (2017). Anisotropy in the lowermost mantle beneath the Indian Ocean Geoid Low from ScS splitting measurements. *Geochemistry, Geophysics, Geosystems*, *18*, 558–570. https://doi.org/10.1002/2016GC006604

Reed, C. A., Gao, S. S., Liu, K. H., & Yu, Y. (2016). The mantle transition zone beneath the Afar Depression and adjacent regions: Implications for mantle plume and hydration. *Geophysical Journal Intertional*, *205*, 1756–1766. https://doi.org/10.1093/gji/ggw116

Richards, M. A., & Griffiths, R. W. (1988). Deflection of plumes by mantle shear flow: Experimental results and a simple theory. *Geophysical Journal*, *94*, 367–376. https://doi.org/10.1111/j.1365-246x.1988.tb02260.x

Ritsema, J., Deuss, A., van Heijst, H. J., & Woodhouse, J. H. (2011). S40RTS: A degree-40 shear-velocity model for the mantle from new Rayleigh wave dispersion, teleseismic traveltime and normal-mode splitting function measurements. *Geophysical Journal International*, *184*, 1223–1236. https://doi.org/10.1111/j.1365-246x.2010.04884.x

Ritsema, J., van Heijst, H. J., & Woodhouse, J. H. (1999). Complex shear wave velocity structure imaged beneath Africa and Iceland. *Science*, *286*(5446), 1925–1928. https://doi.org/10.1126/science.286.5446.1925

Rogers, N., Macdonald, R., Fitton, J. G., George, R., Smith, M., & Barreiro, B. (2000). Two mantle plumes beneath the East African Rift system: Sr, Nd and Pb isotope evidence from Kenya Rift basalts. *Earth and Planetary Science Letters*, *176*, 387–400. https://doi.org/10.1016/s0012-821x(00)00012-1

Rooney, T. O., Hanan, B. B., Graham, D. W., Furman, T., Blichert-Toft, J., & Schilling, J.-G. (2012). Upper mantle pollution during Afar plume-continental rift interaction. *Journal of Petrology*, *53*, 365–389. https://doi.org/10.1093/petrology/egr065

Rooney, T. O., Herzberg, C., & Bastow, I. D. (2012). Elevated mantle temperature beneath East Africa. *Geology*, *40*, 27–30. https://doi.org/10.1130/g32382.1

Rychert, C. A., Hammond, J. O. S., Harmon, N., Kendall, J. M., Keir, D., Ebinger, C., et al. (2012). Volcanism in the Afar Rift sustained by decompression melting with minimal plume influence. *Nature Geoscieince*, *5*, 406–409. https://doi.org/10.1038/ngeo1455

Schubert, G., Masters, G., Olson, P., & Tackley, P. (2004). Superplumes or plume clusters? *Physics of the Earth and Planetary Interiors*, *146*, 147–162. https://doi.org/10.1016/j.pepi.2003.09.025

Schubert, G., Turcotte, D. L., & Olson, P. (2001). *Mantle convection in the Earth and planets*. New York: Cambridge Univ. Press.

Simmons, N. A., Forte, A. M., & Grand, S. P. (2007). Thermochemical structure and dynamics of the African superplume. *Geophysical Research Letters*, *34*, L02301. https://doi.org/10.1029/2006GL028009

Skilbeck, J. N., & Whitehead, J. A. Jr. (1978). Formation of discrete islands in linear island chains. *Nature*, *272*, 499–501. https://doi.org/10.1038/272499a0

Steinberger, B., & Antretter, M. (2006). Conduit diameter and buoyant rising speed of mantle plumes: Implications for the motion of hot spots and shape of plume conduits. *Geochemistry, Geophysics, Geosystems*, *7*, Q11018. https://doi.org/10.1029/2006GC001409

Styles, E., Goes, S., van Keken, P. E., Ritsema, J., & Smith, H. (2011). Synthetic images of dynamically predicted plumes and comparison with a global tomographic model. *Earth and Planetary Science Letters*, *311*, 351–363. https://doi.org/10.1016/j.epsl.2011.09.012

Tan, E., Gurnis, M., & Han, L. (2002). Slabs in the lower mantle and their modulation of plume formation. *Geochemistry, Geophysics, Geosystems*, *3*, 1067. https://doi.org/10.1029/2001GC000238

Tauzin, B., Debayle, E., & Wittlinger, G. (2010). Seismic evidence for a global low-velocity layer within the Earth's upper mantle. *Nature Geoscience*, *3*, 718–721. https://doi.org/10.1038/ngeo969

Thompson, D. A., Hammond, J. O. S., Kendall, J.-M., Stuart, G. W., Helffrich, G. R., Keir, D., et al. (2015). Hydrous upwelling across the mantle transition zone beneath the Afar Triple Junction. *Geochemistry, Geophysics, Geosystems*, *16*, 834–846. https://doi.org/10.1002/2014GC005648

Van der Voo, R., Spakman, W., & Bijwaard, H. (1999). Tethyan subducted slabs under India. *Earth and Planetary Science Letters*, *171*, 7–20. https://doi.org/10.1016/s0012-821x(99)00131-4

Vicente de Gouveia, S., Besse, J., Frizon de Lamotte, D., Greff-Lefftz, M., Lescanne, M., Gueydan, F., & Leparmentier, F. (2018). Evidence of hotspot paths below Arabia and the Horn of Africa and consequences on the Red Sea opening. *Earth and Planetary Science Letters*, *487*, 210–220. https://doi.org/10.1016/j.epsl.2018.01.030

Wessel, P., Smith, W. H. F., Scharroo, R., Joachum, L., & Wobbe, F. (2013). Generic Mapping Tools: Improved version released. *Eos, Transactions of the American Geophysical Union*, *94*(45), 409–410. https://doi.org/10.1002/2013eo450001

Weston, J., Ferreira, A. M. G., & Funning, G. J. (2011). Global compilation of interferometric synthetic aperture radar earthquake source models: 1. Comparisons with seismic catalogs. *Journal of Geophysical Research*, *116*, B08408. https://doi.org/10.1029/2010JB008131

Young, A., Flament, N., Maloney, K., Williams, S., Matthews, K., Zahirovic, S., & Müller, R. D. (2019). Global kinematics of tectonic plates and subduction zones since the late Paleozoic Era. *Geoscience Frontiers*, *10*, 989–1013. https://doi.org/10.1016/j.gsf.2018.05.011